A centralised approach for aerial manipulation on overhanging surfaces

Thesis Report

Martijn Brummelhuis

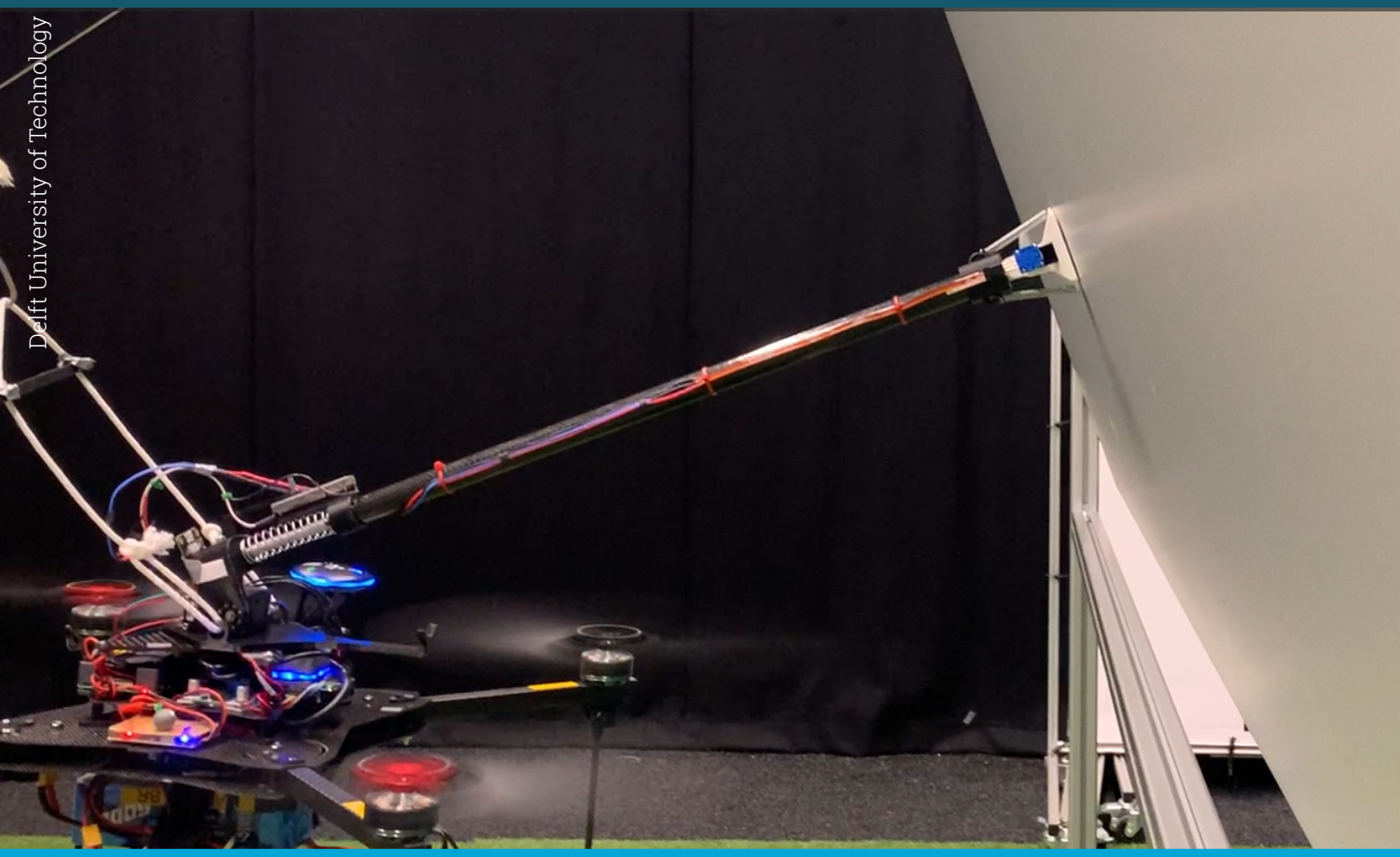

Delft University of Technology

TU Delft

A centralised approach for aerial manipulation on overhanging surfaces

Thesis Report

by

Martijn Brummelhuis

to obtain the degree of Master of Science
at Delft University of Technology, faculty of Aerospace Engineering,
to be defended publicly on April 21, 2023 at 13:00.

Student number:	4442164	
Project duration:	September 2021 - April 2023	
Thesis committee:	Prof. Dr. G.H.C.E. (Guido) De Croon	TU Delft, Chair
	Dr. S. (Salua) Hamaza	TU Delft, Daily Supervisor
	Dr. ir. E.J.J. (Ewoud) Smeur	TU Delft, Additional Supervisor
	Dr. I. (Ivan) Langella	TU Delft, External Examiner

TU Delft

Preface

The document you are reading now contains the work done for my master thesis project at Delft University of Technology. When I started there was no defined, running project going on so there was little established context which allowed me a lot of freedom to define my own project. Working with Internet-of-Things technology in my part-time work made me think about the deployment of such networks using robots, as the work is often done at height or in other inaccessible or dangerous locations. This idea was the main driver behind the project when it was conceived.

This thesis report starts with a short introductory chapter detailing the research outline, objectives and goals. Next, the scientific paper detailing this research is presented. After this, a literature study in all breadth, exploring the work that has been done on the topic of aerial manipulation and aerial physical interaction is presented. This study was delivered and assessed separately, but it has been included for completeness' sake. Additional data and relevant details are presented in the appendix.

Apart from the very official and sensible drivers noted above, another one was my personal desire to build robots or drones, to work hands-on with electronics and code and above all: do flight testing. The past years at TU Delft have made me realise that I'm a true engineer, an inventor, a builder, a maker and a creator. I'm thankful I have been able to spend the past 8 years in this environment, where it's not considered a strange, but a cool thing to dedicate your time to building solar powered flying boats or drones with robot arms.

Although the last couple of months have been relatively smooth sailing, getting used to (and even enjoying) doing research was a process with many ups and downs for me. Dr. Salua Hamaza was there to help me through the times that I was on the verge of giving up, and to share in my enthusiasm when something finally worked the way it was supposed to. Salua, thank you for your continuous support, motivating pep talks and all the good suggestions that pointed me in the right directions. I also want to thank Dr. Ewoud Smeur for his role as additional supervisor, helping me debug my simulations and offering feedback on my writing. A final thanks goes out to all the amazing people at the MAVLab, who have made my time tinkering and testing that much easier and more enjoyable.

On a more personal note, I would not have been able to complete this thesis without the ongoing support of my girlfriend Maartje and friends Koen en Lina. Thanks for being there when I needed to vent about this or that frustrating thing, and making sure I'm still doing all the fun things in life while working on this project. Finally I also would like to thank my family and in particular my parents, who I could always fall back on and who helped me get some perspective when I got too absorbed by the academic process of writing and finishing a thesis.

Martijn Brummelhuis
Delft, April 2023

Contents

Nomenclature

Abbreviations

Abbreviation	Definition
ADC	Analog-Digital Converter
CAD	Computer Aided Drawing
CoM	Center of Mass
DOF(s)	Degree(s) of Freedom
HITL	Hardware-in-the-loop
LQR	Linear-Quadratic Regulator
NED	North-East-Down
PCB	Printed Circuit Board
SITL	Software-in-the-loop
UAM	Unmanned Aerial Manipulator
UAV	Unmanned Aerial Vehicle

Symbols

Symbol	Definition	Unit
B	Inertia matrix	[-]
c	Propeller lift/drag coefficient	[-]
C	Coriolis- and Centrifugal matrix	[-]
d	Denavit Hartenberg parameter	[m]
D_d	Desired virtual damping matrix	[kg/s]
e_3	Down-direction vector	[-]
$\mathcal{F}_b$	Body frame of reference	[-]
$\mathcal{F}_e$	End-effector frame of reference	[-]
$\mathcal{F}_I$	Inertial frame of reference	[-]
$\boldsymbol{f}_{ext}$	External forces in generalised coordinates	[N]
$\boldsymbol{f}_{ext,C}$	External forces in Cartesian coordinates	[N]
$\boldsymbol{f}_i$	Control input forces in generalised coordinates	[N]
f_{ri}	Thrust force of rotor i	[N]
F_{q2}	Force estimate on linear slider	[N]
g	Gravitational acceleration	[m/s^2]
$\boldsymbol{g}()$	Vector of generalised gravitational effects	[N]
H^i_j	Homogeneous Transformation Matrix between frame i and j	[-]
I_b	Inertia tensor of base	[kg/m^2]
I_i	Inertia tensor of link i	[kg/m^2]
J	Jacobian	[-]
J^i_P	Position Jacobian with columns up until link i	[-]
J^i_O	Orientation Jacobian with columns up until link i	[-]
$\mathcal{K}$	Total kinetic energy	[J]
$\mathcal{K}_b$	Kinetic energy of the base	[J]
$\mathcal{K}_i$	Kinetic energy of link i	[J]
K_d	Desired virtual stiffness matrix	[N/m]
$\mathcal{L}$	Lagrangian	[J]

Symbol	Definition	Unit
L_i	Length of member i	[m]
m_b	Mass of the base	[kg]
M_d	Desired Virtual mass/inertia matrix	[kg]
m_i	Mass of link i	[kg]
N	Actuator allocation matrix	[-]
n_{exp}	Number of experiments	[-]
$\boldsymbol{p}_b$	Body position in inertial frame	[m]
$\boldsymbol{p}_i$	Position of link i in inertial frame	[m]
$\boldsymbol{p}_e^b$	Position of $\mathcal{F}_e$ in $\mathcal{F}_b$	[m]
$\boldsymbol{p}_i^b$	Position of link i in body frame	[m]
$\boldsymbol{q}$	Manipulator joint positions	[rad]/[m]
q_1	Angular position of joint 1	[rad]
q_2	Stroke position of joint 2	[m]
q_3	Angular position of joint 3	[rad]
r	Denavit-Hartenberg parameter	[m]
r	Distance from vehicle CoM to rotor center	[m]
R_b	Rotation matrix from $\mathcal{F}_b$ to $\mathcal{F}_I$	[-]
$\bar{R}_b$	Extended rotation matrix from $\mathcal{F}_b$ to $\mathcal{F}_I$	[-]
R_e	Rotation matrix from $\mathcal{F}_e$ to $\mathcal{F}_I$	[-]
R_j^i	Rotation matrix between frame i and j	[-]
T_b	Angular velocity transformation matrix	[-]
t	Time	[s]
$\boldsymbol{u}$	Vector of input forces and torques	[N]/[Nm]
$\mathcal{U}$	Total potential energy	[J]
$\mathcal{U}_b$	Potential energy of base	[J]
$\mathcal{U}_i$	Potential energy of link i	[J]
$v_{approach}$	End-effector to wall approach velocity	[m/s]
x_b	Position of $\mathcal{F}_\llcorner$ along inertial x-axis	[m]
x_e	Position of $\mathcal{F}_\urcorner$ along inertial x-axis	[m]
$x_{e,r}$	Reference position of $\mathcal{F}_\urcorner$ along inertial x-axis	[m]
$\boldsymbol{x}_{e,d}$	Desired end-effector pose vector	[m]/[rad]
$\boldsymbol{x}_{e,r}$	Reference end-effector pose vector	[m]/[rad]
y_b	Position of $\mathcal{F}_\llcorner$ along inertial y-axis	[m]
y_e	Position of $\mathcal{F}_\urcorner$ along inertial y-axis	[m]
$y_{e,r}$	Reference position of $\mathcal{F}_\urcorner$ along inertial y-axis	[m]
z_b	Position of $\mathcal{F}_\llcorner$ along inertial z-axis	[m]
z_e	Position of $\mathcal{F}_\urcorner$ along inertial z-axis	[m]
$z_{e,r}$	Reference position of $\mathcal{F}_\urcorner$ along inertial z-axis	[m]
α	Denavit-Hartenberg parameter	[rad]
$\Delta\boldsymbol{x}$	Desired to reference pose offset	[m]/[rad]
θ_b	Body pitch angle	[rad]
θ_e	End-effector pitch angle	[rad]
$\theta_{e,r}$	End-effector pitch angle reference	[rad]
μ	Mean	[-]
$\boldsymbol{\xi}$	State vector	[m]/[rad]
ξ_i	State i in state vector	[m]/[rad]
σ	Standard deviation	[-]
τ_{q1}	Servo torque	[Nm]
$\boldsymbol{\phi}$	Vector of Euler angles	[rad]
φ_b	Body roll angle	[rad]
ψ_b	Body yaw/heading angle	[rad]
ψ_e	End-effector yaw/heading angle	[rad]
$\psi_{e,r}$	End-effector yaw/heading angle reference	[rad]
$\boldsymbol{\omega}_b$	Body angular velocities in inertial frame	[rad/s]

Symbol	Definition	Unit
$\boldsymbol{\omega}_i$	Angular velocities of link i in inertial frame	[rad/s]
$\boldsymbol{\omega}_i^b$	Angular velocities of link i in body frame	[rad/s]

1

Introduction

Unmanned Aerial Vehicles (UAVs) have gained popularity as platforms for surveillance and monitoring, but applications involving aerial physical interaction are still scarce. The research presented here envisions the roll-out of Internet-of-Things sensor networks through the use of Unmanned Aerial Manipulators (UAMs) to automatise this operation in high or inaccessible locations.

In earlier works, the task of sensor installation was tackled only on vertical walls. As such, a research gap of physical interaction on overhanging surfaces (such as under bridge arches) was identified. In addition, previous work favours a decentralised modeling and control approach, where centralised modeling and control holds a potential for better tracking performance. Given these two motivations, the following research objective was established for this work:

"To enable sensor node placement on surfaces of different inclinations ('overhanging surfaces'), by implementing a manipulation system consisting of simple manipulator and a centralised impedance controller on a quadrotor which allows the UAM to reject or counteract the disturbance forces arising from the interaction and impose normal forces (pushing) on the surface."

Following this objective, a main research question along with sub-questions were formulated:

What is the maximum force/weight ratio that can practically be achieved for 20 seconds on surfaces of 90°, 100°, and 110° in tension (installation) by a quadrotor in a point contact task?

- What happens at high platform attitude angles and how can we maintain stability in this situation?
- What kind of controller can be used to achieve compliant interaction and exploit the quadrotor's attitude?
- How can we observe the interaction force at the end-effector?
- Is on-board force feedback necessary and with what accuracy does the force need to be observed?
- How can we generate adequate yaw torque to counteract disturbance moments on this axis?
- How can we determine the inclination of the interaction surface?

The core of this research is about expanding the body of work on centralised modeling and control, and showing an expanded workspace including overhanging surfaces. It is the author's belief that a holistic view of UAMs will lead to controllers that are more informed on a lower level, allowing different parts of the system to work together rather than counteracting each other. While centralised control in itself presents no research gap, the current body of work is very small. A true research gap is addressed by the chosen task of overhanging surface interaction, which was not before shown with a quadrotor and point contact task.

Part I

Scientific paper

Assessed April 2023 for AE5310: Thesis Control and Operations

A centralised control approach to compliant aerial manipulation on overhanging surfaces

M.B.J. Brummelhuis
Delft University of Technology, Faculty of Aerospace Engineering, Department of Control & Simulation, Micro-Air-Vehicle Laboratory (MAVLab), Delft, the Netherlands

ABSTRACT

Aerial physical interaction opens the door for many operations at height to be automatised using aerial robots. This research presents a novel manipulator design mounted on a traditional quadrotor, which utilises both mechanical and software compliance to perform physical interaction on vertical walls and overhanging surfaces, such as those found under bridges. A centralised impedance control scheme allows direct control of the end-effector pose without needing separate modes for free-flight and contact. A spring-loaded prismatic joint provides passive compliance while doubling as a force-feedback for the impedance controller through measuring the spring displacement. Simulation and flight experiments prove the feasibility and robustness of this approach for exchanging high forces at height, with a total of 44 successful experiments carried out in four sets. An average maximum force of 5.66 N or 19.3% of the system's weight was achieved over one set of 11 experiments.

1 INTRODUCTION

Unmanned Aerial Vehicles (UAVs) are increasingly finding a place in society as platforms for monitoring, inspection or surveillance. The applications for which UAVs are currently deployed commercially share the assumption that aerial operations are carried out in a contactless manner [1, 2]. The potential of aerial robots is extended considerably if this assumption is lifted. Despite the complexity of aerial physical interaction, the possibility of combining the boundless workspace of a UAV with the versatile manipulation capacities of a robotic end-effector creates many avenues for increasing safety and reducing cost, especially in industries that require inspection and maintenance in dangerous conditions.

Recently, the digitisation through the Internet of Things ecosystem has enabled the roll-out of wireless sensor networks [3], which may require placement of a considerable number of small sensor modules in inaccessible or high locations. A distinction can be made between direct and indirect sensor placement, where direct placement requires physical interaction and indirect placement employs a 'shoot and stick' [4] or aerial drop method [5]. Direct sensor placement has been tackled in earlier works [6, 7], but has been limited to the placement on vertical walls using highly custom (that is, not generalisable) manipulator and controller designs that cannot deal with varying inclinations of interaction surfaces.

In this work, the task of direct sensor placement is formalised in the task domain, where the aerial robot and manipulator onboard behave as a single mobile entity with paired dynamics. This centralised control strategy also favours the system's applicability to other tasks conducted airborne, such as non-destructive testing on large infrastructure [8, 9].

Force exertion by an aerial manipulator has been addressed by previous works that have shown that the quadrotor attitude can be exploited to exert substantial and sustained force on vertical surfaces. To deal with the extreme attitude angles involved, a continuous gain-scheduling Linear-Quadratic Regulator (LQR) controller was implemented [10]. A common way of dealing with the contact forces arising is through an impedance-based controller on the manipulator. A distinction can be made between centralised and decentralised control schemes, where in centralised schemes the drone-manipulator system or unmanned aerial manipulator (UAM) is regarded as one integrated system and in decentralised schemes the drone and manipulator are regarded as separate systems, with control inaccuracies and moving mass effects being interpreted as disturbances.

Earlier work on centralised modelling has shown the general derivation of equations of motion through the Euler-Lagrange formalism along with simulation results [11]. Flight tests were performed with this scheme applied to a ducted-fan drone [12]. Another centralised impedance scheme, which was very influential in this research, was proposed for a quadrotor with 6 degrees-of-freedom (DOFs) serial manipulator [13]. This work was subsequently expanded into a selective impedance controller [14] using a fully-actuated platform, where the different inertial dimensions are allocated different impedance characteristics based on the intended application. A 'flying end-effector paradigm' was introduced based on the centralised framework [15], which is a philosophy that is followed in this research by controlling the end-effector pose directly. In the cited work, the scheme is combined with an admittance-based controller. Where previous works tend towards fully-actuated platforms to achieve the desired compliance through software means, the system proposed here employs a manipulator design featuring a lin-

ear spring to provide passive compliance and force feedback for the impedance controller. This is an underactuated implementation of the controller presented in [13].

The efficacy of a combination of passive (mechanical) and active (software) compliance was shown by Suarez *et al.* [16, 17]. Here, the integration of springs combined with position measurement was used to estimate payload mass, where in this work it is used to estimate interaction force.

The contributions of this work are the novel compliant manipulator design with integrated force estimation via constant spring stiffness and the formulation of the coupled dynamics paired with a centralised impedance control scheme. Additionally, simulation results and an extensive experimental analysis on a real prototype validate the approach on both vertical and overhanging surfaces. In achieving this, we show the benefit of mechanical and virtual compliance, the first employed in the robot via a linear spring, the latter via impedance control.

An overview of the manipulator design along with motivations for the design decisions is given in section 2. The methodology of derivation and the resulting model are given in section 3, along with definitions and conventions used in this paper. In section 4 the centralised impedance controller is introduced. The system and controller were jointly simulated for validation, detailed in section 5 along with simulation results and analysis. The flight experiments and associated results and analysis are documented in section 6. The paper is concluded by section 7.

2 System Design

The flying base used in this research is a quadrotor with parallel propellers.

The custom manipulator is mounted on top of the drone. The manipulator features three links (excluding the drone/base link) and three joints, of which two are rotary and one is prismatic. Joints are numbered from the base to the end-effector, starting at 1. Only the first joint is actuated, the other two are spring-loaded but not actively controlled, and monitored using commonly available potentiometers. A Computer Aided Drawing (CAD) model of the manipulator is shown in Figure 1 and the prototype is shown in Figure 2.

The joint definitions in the kinematic chain are shown in Figure 3. From the base, the first joint (denoted q_1) is an actively controlled rotary joint consisting of a Dynamixel XH430-W210 servo. The choice here is twofold: using the servo the pitch angle of the manipulator is decoupled from the drone's pitch angle and the servo extends the workspace of the manipulator to include overhanging surfaces.

The second prismatic joint is guided by an aluminium rod through a linear ball bearing located in the carbon fibre tube, and is equipped with a linear potentiometer to measure stroke on the passive slider. The prismatic joint doubles as embedded mechanical compliance and force estimation

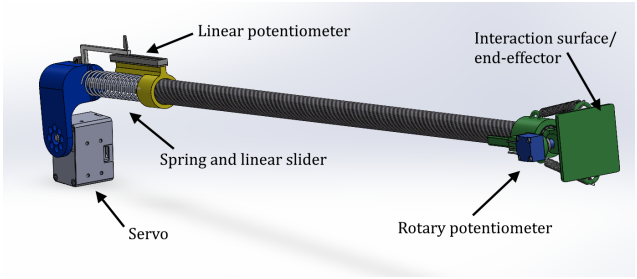

Figure 1: Detailed CAD model of the 3 DOFs manipulator (PCBs and cables not shown).

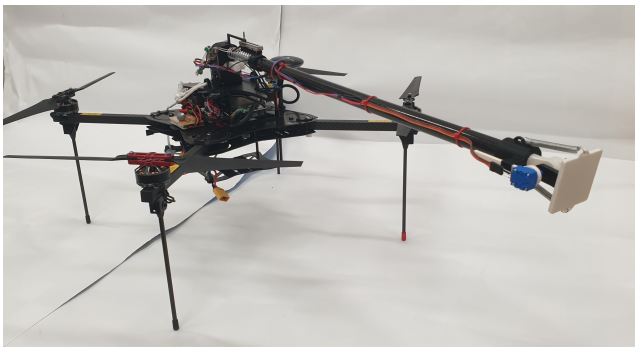

Figure 2: Compliant aerial manipulator prototype built for the experiments.

through the known spring stiffness.

The third rotary joint is passive but spring loaded such that when the manipulator is not in contact, the end-effector remains in its nominal position. Since sensor placement is essentially a planar contact task, this compliant joint favours position uncertainty about the interaction plane, by providing a buffer of $\pm 20°$ in the case the end-effector's interaction plane is not immediately tangential to the target at contact. Additionally, by sensing the angular position of the joint, the controller knows the plane inclination when contact is established.

3 Modeling

In this section the controller model is described, applied directly to the system described above, to provide an example

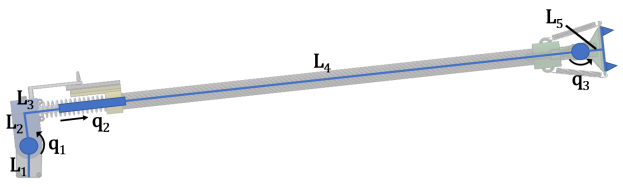

Figure 3: Kinematic diagram of the manipulator.

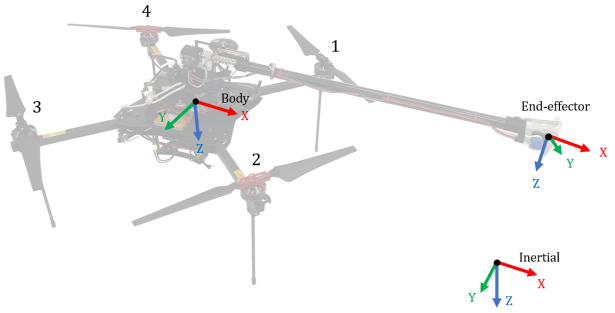

Figure 4: Definition of the inertial-, body- and end-effector reference frames, and rotor numbering.

of centralised modeling. First conventions and notations are introduced, then the derivation of the kinematics is shown and ultimately the dynamic model is derived using the Euler-Lagrange formalism.

3.1 Conventions, notation and definitions

Vectors are denoted in bold and matrices are denoted by capital letters, while lower-case letters stand for scalar variables.

The main reference frames used are the inertial frame $\mathcal{F}_I$, the body frame $\mathcal{F}_b$ and the end-effector frame $\mathcal{F}_e$. The NED (North-East-Down) convention is followed for $\mathcal{F}_I$. $\mathcal{F}_b$ is defined body-fixed, with the origin O_b at the UAM's center of mass (CoM). X_b is positive forward between rotors 1 and 2, Y_b is positive right, between rotors 2 and 3, and Z_b is positive down. $\mathcal{F}_e$ is defined with X_e normal to the interaction plane, the positive direction away from the end-effector into the wall. Z_e is defined positive down in the nominal configuration and Y_e follows from the right-handedness of the frame. Figure 4 shows the frame definitions and rotor numbering. The set of Euler angles is denoted $\boldsymbol{\phi}_b = [\psi_b \ \theta_b \ \varphi_b]^\top$ for yaw (around Z_b), pitch (around Y_b) and roll (around X_b), respectively. The rotation matrix is given by

$$R_b = \begin{bmatrix} c\theta c\psi & s\varphi s\theta c\psi - c\varphi s\psi & c\varphi s\theta c\psi + s\varphi s\psi \\ c\theta s\psi & s\varphi s\theta s\psi + c\varphi c\psi & c\varphi s\theta s\psi - s\varphi c\psi \\ -s\theta & s\varphi c\theta & c\varphi c\theta \end{bmatrix} \tag{1}$$

and converts a vector from the body frame to the inertial frame through premultiplication [12]. For brevity's sake, $s\psi$ denotes $\sin(\psi_b)$ and $c\psi$ denotes $\cos(\psi_b)$ and similarly for θ_b and φ_b.

The time derivative of the Euler angles holds no physical significance due to the order of rotations. This causes the unit vectors associated with $\dot{\boldsymbol{\phi}}$ to become non-orthogonal. Therefore, the transformation

$$\boldsymbol{\omega}_b = T_b \dot{\boldsymbol{\phi}}_b = \begin{bmatrix} 0 & -s\theta & c\theta c\psi \\ 0 & c\psi & c\theta s\psi \\ 1 & 0 & -s\theta \end{bmatrix} \begin{bmatrix} \dot{\psi} \\ \dot{\theta} \\ \dot{\varphi} \end{bmatrix} \tag{2}$$

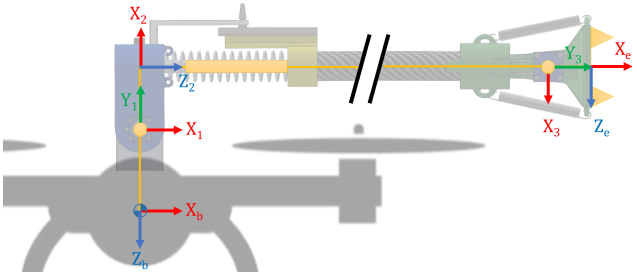

Figure 5: Denavit-Hartenberg frames on the manipulator.

is introduced to convert between the Euler angles' time derivative and angular velocities [12, 18].

The generalised coordinates $\boldsymbol{\xi}$ are defined as the six-dimensional full pose of the base (positions $\boldsymbol{p}_b = [x_b \ y_b \ z_b]^\top$ and orientations $\boldsymbol{\phi}_b = [\varphi_b \ \theta_b \ \psi_b]^\top$) concatenated with the joint angles ($\boldsymbol{q} = [q_1 \ q_2 \ q_3]^\top$ of the manipulator. This yields the following definition for the generalised coordinates:

$$\begin{aligned} \boldsymbol{\xi} &= \begin{bmatrix} \boldsymbol{p}_b & \boldsymbol{\phi}_b & \boldsymbol{q} \end{bmatrix}^\top \in \mathbb{R}^n \\ &= \begin{bmatrix} x_b & y_b & z_b & \psi_b & \theta_b & \varphi_b & q_1 & q_2 & q_3 \end{bmatrix}^\top, \end{aligned} \tag{3}$$

where x_b, y_b and z_b denote the position of O_b in $\mathcal{F}_I$ and ψ_b, θ_b and φ_b are the Euler angles. For the manipulator's coordinates, q_1 and q_3 represent revolute joints and q_2 represents the prismatic joint. These are visually clarified in Figure 3.

3.2 Kinematics

The kinematics of the robot are derived in two parts using the homogeneous transformation matrix. A transformation from $\mathcal{F}_b$ to $\mathcal{F}_I$ is established as shown in Equation 4a. The transformations of the manipulator are done link-by-link and by following the Denavit-Hartenberg convention. The kinematic diagram along with the frames attached to the joints is shown in Figure 3. The associated Denavit-Hartenberg parameters are given in Table 1.

Table 1: Denavit-Hartenberg parameters of the manipulator.

Joint	$\boldsymbol{\theta}$	$\boldsymbol{\alpha}$	$\boldsymbol{r}$	$\boldsymbol{d}$
1	0	$-\frac{\pi}{2}$	0	$-L_1$
2	$\frac{\pi}{2} + q_1$	$\frac{\pi}{2}$	L_2	0
3	π	$\frac{\pi}{2}$	0	$q_2 + L_3 + L_4$
E	$\frac{\pi}{2} + q_3$	$\frac{\pi}{2}$	L_5	0

The homogeneous transformation matrices following from these parameters are documented in Appendix A:. The obtained homogeneous transformation matrices can then be multiplied to obtain a single equivalent homogeneous transformation matrix from $\mathcal{F}_e$ to $\mathcal{F}_I$:

$$H_b^I = \begin{bmatrix} R_b & \boldsymbol{p}_b \\ \boldsymbol{0}^\top & 1 \end{bmatrix} \tag{4a}$$

$$H_e^b = \begin{bmatrix} R_e^b & \boldsymbol{p}_e^b \\ \boldsymbol{0}^\top & 1 \end{bmatrix} \tag{4b}$$

$$H_e^I = H_b^I H_e^b, \tag{4c}$$

where H_e^I denotes the transformation from $\mathcal{F}_e$ to $\mathcal{F}_I$. From this form, the kinematics can be expressed in the form of a vector equation [19]. This form is useful for later calculation of the Jacobian. The conversion from the entries of the homogeneous transformation matrix to the vector equation describing the end-effector pose $\boldsymbol{x}_e$ as a function of $\boldsymbol{\xi}$ is done by applying

$$\boldsymbol{k}(\boldsymbol{\xi}) = \boldsymbol{x}_e = \begin{bmatrix} x_e & y_e & z_e & \psi_e & \theta_e & \varphi_e \end{bmatrix}^\top \tag{5a}$$

$$x_e = H_e^I(1,4) \tag{5b}$$

$$y_e = H_e^I(2,4) \tag{5c}$$

$$z_e = H_e^I(3,4) \tag{5d}$$

$$\psi_e = \arctan(H_e^I(2,1)/H_e^I(1,1)) \tag{5e}$$

$$\theta_e = -\arcsin(H_e^I(3,1)) \tag{5f}$$

$$\varphi_e = \arctan(H_e^I(3,2)/H_e^I(3,3)), \tag{5g}$$

where $H(i,j)$ denotes the entry at row i and column j of the homogeneous transformation matrix. The resulting kinematics equation is presented in Appendix A:.

Once determined, $\boldsymbol{k}(\boldsymbol{\xi})$ can be derived with respect to the state to find the system's Jacobian, which relates the end-effector velocity to the first time derivative of the generalised coordinates through the differential kinematics,

$$\dot{\boldsymbol{x}}_e = J\dot{\boldsymbol{\xi}} = \frac{\partial \boldsymbol{k}(\boldsymbol{\xi})}{\partial \boldsymbol{\xi}} \dot{\boldsymbol{\xi}}. \tag{6}$$

The full Jacobian expression can be found in Appendix A:.

To calculate link velocities, a reference frame is introduced at the CoM of each link. This link reference frame is attached with its origin at the CoM of each link, with the axes aligning with the principal axes of inertia of the link such that the inertia tensor remains diagonal. The position of a link i can be expressed as

$$\boldsymbol{p}_i = \boldsymbol{p}_b + R_b \boldsymbol{p}_i^b, \tag{7}$$

where $\boldsymbol{p}_i^b$ denotes the position of link i in $\mathcal{F}_b$. This vector was populated for each of the three links of the manipulator individually, by utilising the symmetry of the links where possible and determining the position relative to the closest joint frame as used by the Denavit-Hartenberg convention (since these frames have known positions and orientations). Deriving Equation 7 with respect to time and taking into account [19]

$$\dot{\boldsymbol{p}}_i^b = J_{P1}^i \dot{q}_1 + ... + J_{Pi}^i \dot{q}_i = J_P^{li} \dot{\boldsymbol{q}} \tag{8a}$$

$$\boldsymbol{\omega}_i^b = J_{O1}^i \dot{q}_1 + ... + J_{Oi}^i \dot{q}_i = J_O^{li} \dot{\boldsymbol{q}}, \tag{8b}$$

yields the link velocities [11]

$$\dot{\boldsymbol{p}}_i = \dot{\boldsymbol{p}}_b - S(R_b \boldsymbol{p}_i^b)\boldsymbol{\omega}_b + R_b J_P^{(i)} \dot{\boldsymbol{q}} \tag{9a}$$

$$\boldsymbol{\omega}_i = \boldsymbol{\omega}_b + R_b J_O^{(i)} \dot{\boldsymbol{q}}. \tag{9b}$$

The terms J_P^i and J_O^i denote the columns of the manipulator Jacobian (not the full Jacobian of Equation 6) up until link i, with subscript P meaning the first three rows (associated with position) and subscript O meaning the bottom three rows (associated with orientation). These expressions were also derived individually per link, as the Jacobian of Equation 6 involves velocities at the joint reference frame origin (the reference frames at the joints used in the kinematics), but for the dynamic model the CoM position and velocity of the links are required.

3.3 Dynamics

The Euler-Lagrange formalism is used to model the system dynamics. The Lagrangian is calculated using the following equation:

$$\mathcal{L} = \mathcal{K}(\dot{\boldsymbol{\xi}}, \boldsymbol{\xi}) - \mathcal{U}(\boldsymbol{\xi}). \tag{10}$$

The kinetic energy of the system is found by

$$\begin{aligned} \mathcal{K} &= \mathcal{K}_b + \sum_{i=1}^{n} \mathcal{K}_i \\ &= \frac{1}{2} m_b \dot{\boldsymbol{p}}_b^\top \dot{\boldsymbol{p}}_b + \frac{1}{2} \boldsymbol{\omega}_b^\top R_b I_b R_b^\top \boldsymbol{\omega}_b \\ &+ \frac{1}{2} \sum_{i=1}^{3} \left(m_i \dot{\boldsymbol{p}}_i^\top \dot{\boldsymbol{p}}_i + \boldsymbol{\omega}_i^\top R_i I_i R_i^\top \boldsymbol{\omega}_i \right). \end{aligned} \tag{11}$$

In this equation $\mathcal{K}$ denotes the system's total kinetic energy, $\mathcal{K}_b$ denotes the base's kinetic energy and $\mathcal{K}_i$ denotes the kinetic energy of the i^{th} link.

The rotation matrices of the CoM frames of the links were determined individually for each link, reasoning from the closest (i.e. last from the base) joint-fixed kinematics frame that has a known rotation matrix from the homogeneous transformation matrix. Link inertias were found from the manipulator's CAD model.

Similar to the kinetic energy, the potential energy can be calculated link-wise by applying

$$\begin{aligned} \mathcal{U} &= \mathcal{U}_b + \sum_{i=1}^{n} \mathcal{U}_i \\ &= m_b g \boldsymbol{e}_3 \boldsymbol{p}_b + \sum_{i=1}^{3} m_i g \boldsymbol{e}_3 \boldsymbol{p}_i, \end{aligned} \tag{12}$$

where $\mathcal{U}$ denotes the system's total potential energy, $\mathcal{U}_b$ denotes the potential energy of the base and $\mathcal{U}_i$ denotes the potential energy of link i. The gravitational acceleration g equals $9.81\ m/s^2$ and vector $\boldsymbol{e}_3$ is $[0\ 0\ 1]$, for selecting the z-coordinate of the base and each link.

The equations of motion of the system can be found from the Lagrangian by applying

$$\frac{d}{dt}\frac{\partial \mathcal{L}}{\partial \dot{\xi}_i} - \frac{\partial \mathcal{L}}{\partial \xi_i} = u_i \tag{13}$$

for each generalised coordinate, yielding n equations of motion describing the full system dynamics. In this equation, $\mathcal{L}$ denotes the system Lagrangian, ξ_i refers to the i^{th} generalised coordinate and u_i is the generalised external force associated with that generalised coordinate.

Applying this series of mathematical operations to a robotic manipulator (whether it's fixed-base or floating-base) yields equations of motion following a similar structure. In matrix-form they can be expressed as [20]

$$B(\boldsymbol{\xi})\ddot{\boldsymbol{\xi}} + C(\dot{\boldsymbol{\xi}}, \boldsymbol{\xi})\dot{\boldsymbol{\xi}} + \boldsymbol{g}(\boldsymbol{\xi}) = \boldsymbol{f}_i + \boldsymbol{f}_{ext}. \tag{14}$$

In this equation, $B(\boldsymbol{\xi}) \in \mathbb{R}^{(n\times n)}$ is the symmetric, positive-definite generalised inertia matrix, also sometimes referred to as the mass matrix. The Coriolis and centrifugal terms are represented by $C(\dot{\boldsymbol{\xi}}, \boldsymbol{\xi}) \in \mathbb{R}^{(n\times n)}$, the generalised gravitational effects are defined by $\boldsymbol{g}(\boldsymbol{\xi}) \in \mathbb{R}^n$. For the system discussed here, $n = 9$. On the right-hand side of the equation all non-conservative terms (i.e. generalised forces that add or dissipate energy in the system) are grouped, split into $\boldsymbol{f}_i$ as the term of control inputs and $\boldsymbol{f}_{ext}$ for all external forces acting on the system.

Lippiello and Ruggiero [11] show the derivation of the equations of motion in the form of Equation 14 through the Euler-Lagrange formalism for UAMs with single, serial manipulators in a general way. Going from their derivation provides computational cost savings because Equation 13 does not have to be derived explicitly. The reasoning starts by recalling that the kinetic energy of the system can also be expressed as

$$\mathcal{K} = \frac{1}{2}\dot{\boldsymbol{\xi}}^\top B \dot{\boldsymbol{\xi}}, \tag{15}$$

and isolating B by separating terms that are linearly dependent on the elements of $\dot{\boldsymbol{\xi}}$. This derivation yields a computationally inexpensive method of determining the block elements of B, described by Lippiello and Ruggiero [11]. With $B(\boldsymbol{\xi})$ known, the Coriolis and centrifugal matrix $C(\dot{\boldsymbol{\xi}}, \boldsymbol{\xi})$ can be found by observing the *Christoffel symbols of the first type* [19]:

$$C_{ij} = \frac{1}{2}\sum_{k=1}^{n}\left(\frac{\partial B_{ij}}{\partial \xi_k} + \frac{\partial B_{ik}}{\partial \xi_j} - \frac{\partial B_{jk}}{\partial \xi_i}\right)\dot{\xi}_k. \tag{16}$$

Here, C_{ij} represents the element of C at row i and column j, and similarly for B, while ξ_k represents the k^{th} entry of $\boldsymbol{\xi}$. By recalling that $\mathcal{U}$ does not depend on $\dot{\boldsymbol{\xi}}$, it can be shown from the Euler-Lagrange equation that the gravitational effects in the manipulator equation can be calculated as

$$\boldsymbol{g}(\boldsymbol{\xi}) = -\frac{\partial \mathcal{U}}{\partial \boldsymbol{\xi}}. \tag{17}$$

The actuator forces in the right-hand side of Equation 14 are given by [11]:

$$\boldsymbol{f}_i = \bar{R}_b N \boldsymbol{u}, \tag{18}$$

with $\bar{R}_b = diag(R_b, R_b T_b^\top, I_3)$, a matrix rotating all forces from $\mathcal{F}_b$ to $\mathcal{F}_I$ and $\boldsymbol{u} = [f_{r1}\ f_{r2}\ f_{r3}\ f_{r4}\ \tau_{q1}]^\top$, the vector stacking all input forces and torques. N denotes the allocation matrix, which for this configuration is

$$N = \begin{bmatrix} 0 & 0 & 0 & 0 & 0 \\ 0 & 0 & 0 & 0 & 0 \\ -1 & -1 & -1 & -1 & 0 \\ -c & c & -c & c & 0 \\ \frac{1}{2}\sqrt{r} & \frac{1}{2}\sqrt{r} & -\frac{1}{2}\sqrt{r} & -\frac{1}{2}\sqrt{r} & 0 \\ \frac{1}{2}\sqrt{r} & -\frac{1}{2}\sqrt{r} & -\frac{1}{2}\sqrt{r} & \frac{1}{2}\sqrt{r} & 0 \\ 0 & 0 & 0 & 0 & 1 \\ 0 & 0 & 0 & 0 & 0 \\ 0 & 0 & 0 & 0 & 0 \end{bmatrix}. \tag{19}$$

In this expression, c is the lift/drag ratio of the propeller and r is the distance between O_b and the rotor center.

The external force on the manipulator needs to be mapped to Cartesian and generalised coordinates, from the measurement on q_2. A conversion between the Cartesian six-dimensional coordinates and the nine-dimensional generalised coordinates is given by Cataldi *et al.* [13],

$$\boldsymbol{f}_{ext} = \begin{bmatrix} \boldsymbol{I}_{(3\times3)} & \boldsymbol{O}_{(3\times3)} \\ T_b^\top S(\boldsymbol{p}_e^b) & T_b^\top \\ [J_{man}^b]^\top \end{bmatrix} \boldsymbol{f}_{ext,C}. \tag{20}$$

In this expression, $S()$ means the skew-symmetric matrix of the input vector and J_{man}^b represents the manipulator Jacobian. This is the Jacobian of the manipulator as if the drone is a static base and $\mathcal{F}_b$ acts as the inertial frame. Furthermore, $\boldsymbol{f}_{ext,C}$ stands for the external force in the six-dimensional Cartesian space, expressed in $\mathcal{F}_I$. It can be calculated from the force estimate of the prismatic joint by

$$\boldsymbol{f}_{ext,C} = \begin{bmatrix} R_e & \boldsymbol{O}_{(3\times3)} \\ \boldsymbol{O}_{(3\times3)} & R_e \end{bmatrix} \begin{bmatrix} \cos(q_3) \\ 0 \\ -\sin(q_3) \\ \boldsymbol{O}_{(1\times3)} \end{bmatrix} f_{q2}, \tag{21}$$

where f_{q2} is the force on the prismatic joint and R_e the rotation matrix from $\mathcal{F}_e$ to $\mathcal{F}_I$:

4 Controller

In order to successfully complete the task of applying a sustained force to a varying-inclination overhang surface, the impedance controller from [13] was adapted and implemented on the system.

This controller has a hierarchical layered structure with three layers, displayed in Figure 6 (the subpart labeled 'controller'). The top layer, called the impedance layer, takes a desired end-effector pose setpoint and (if present) the external force on the end-effector as sensed by joint q_2. It outputs an adjusted end-effector pose setpoint computed through

$$M_d\Delta\ddot{\boldsymbol{x}} + D_d\Delta\dot{\boldsymbol{x}} + K_d\Delta\boldsymbol{x} = \boldsymbol{f}_{ext,C}, \tag{22}$$

which is called the impedance equation [13]. This filter causes the end-effector to behave like a mass-spring-damper system with properties as defined in the positive definite (and usually diagonal) M_d, D_d and K_d matrices. The $\Delta\boldsymbol{x}$ and its time derivatives represent the difference between the desired setpoint (received by the impedance layer) $\boldsymbol{x}_{e,d}$ and the reference generated by the impedance layer $\boldsymbol{x}_{e,r}$: $\Delta\boldsymbol{x} = \boldsymbol{x}_{e,d} - \boldsymbol{x}_{e,r}$.

The second layer uses the generated end-effector pose setpoint and decomposes it into references for the controlled states, which is the subset of the system state that can be controlled by the actuators in the system. For this system, these are the states x, y, z, ψ (the drone position and heading) and q_1 (the servo position). This was achieved by a simple algebraic rewriting of the forward kinematics, where the uncontrolled states were assumed to be zero. This assumption was deemed valid as the setpoints of the drone and manipulator for these states are zero and were expected to deviate little from this value. A pitch compensation term was added to the calculation of the servo position to make it compensate for the varying pitch of the drone during interaction. The position inverse kinematics are expressed as functions of the link lengths and elements of $\boldsymbol{x}_{e,r}$ by

$$\begin{aligned} x = {} & x_{e,r} - \cos(\psi_{e,r})(L_3\cos(\theta_{e,r}) + \\ & L_4\cos(\theta_{e,r}) + L_5\cos(\theta_{e,r}) - L_2\sin(\theta_{e,r})) \end{aligned} \tag{23a}$$

$$\begin{aligned} y = {} & y_{e,r} - \sin(\psi_{e,r})(L_3\cos(\theta_{e,r}) + \\ & L_4\cos(\theta_{e,r}) + L_5\cos(\theta_{e,r}) - L_2\sin(\theta_{e,r})) \end{aligned} \tag{23b}$$

$$\begin{aligned} z = {} & z_{ee} + L_1 + L_2\cos(\theta_{e,r}) + L_3\sin(\theta_{e,r}) + \\ & L_4\sin(\theta_{e,r}) + L_5\sin(\theta_{e,r}) \end{aligned} \tag{23c}$$

$$\psi = \psi_{e,r} \tag{23d}$$

$$q_1 = \theta_{e,r} - \theta_b \tag{23e}$$

The final layer is a position controller that tracks the references for the controlled states. Since the proposed system has only five actuators (four rotors and one servo), full pose control of the end-effector is not possible. For this reason, roll angle control on the end-effector is relinquished as it will by default stay close to 0° in semi-static interaction, to keep the drone platform in a constant lateral position.

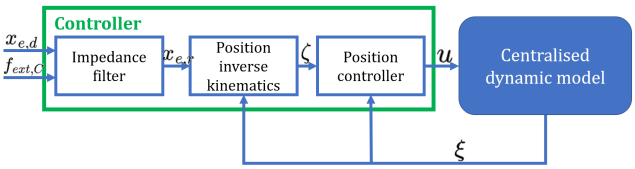

Figure 6: Controller and simulation block diagram.

5 Simulation

In order to validate the controller before implementation on flight hardware, the controller and centralised model were tested in simulation. A block diagram of the simulation can be found in Figure 6. It should be noted that since physical parameters of the platform used in the flight experiments were not known yet, therefore other parameters from similar systems were taken as reference for the simulated model [13].

5.1 *End-effector position tracking*

A simple hierarchical position controller was implemented such that the controlled variables are the 3-dimensional position of the drone along with the heading. This position controller was tuned with the full model including manipulator such that references on the controlled variables can be followed and the platform would remain stable. An end-effector position tracking mission was simulated by setting a step input on the references of the position coordinates.

Results of the end-effector position tracking simulation experiment are shown in Figure 7. In this experiment a step input is given on the end-effector position. From the result plots it is clear that x_e and z_e oscillate slightly which is mainly attributed to the presence of the manipulator in the model. It should be noted that the model was found to be quite hard to control using this simple position controller, as it had a tendency to experience loss of control when sudden changes on the references were present. This is mainly attributed due to the addition of the manipulator in the model, which exchanges momentum with the drone body when moving, introducing disturbances on the body that are hard to reject for the position controller.

5.2 *End-effector orientation tracking*

To show orientation tracking on the end-effector frame through the proposed controller, time-varying references for the end-effector pitch are given, while the position remains constant. This means the controller should command the drone to move around the end-effector to keep the end-effector position constant while changing the pitch to follow

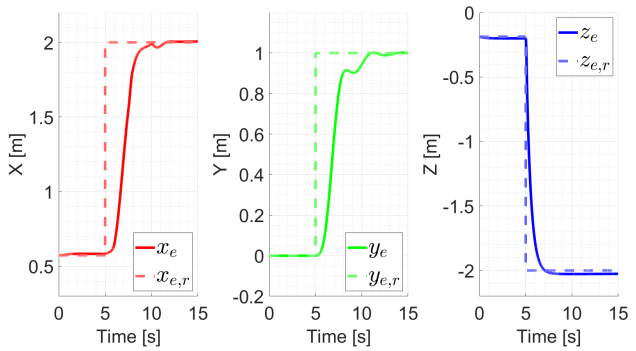

Figure 7: Simulated end-effector inertial position response and references.

the references appropriately, see Figure 8. Additional results showing the movement of the drone body around the end-effector location are presented in Appendix B:.

It was shown that the end-effector is able to effectively track a time-varying pitch trajectory. This trajectory was chosen because it shows the centralised control approach through servo reference generation. Simultaneously tracking a step reference on the heading demonstrates the robustness of the orientation control. In the additional results, it can be seen that the drone body moves up, down and sideways to maintain end-effector location, validating the inverse kinematics layer.

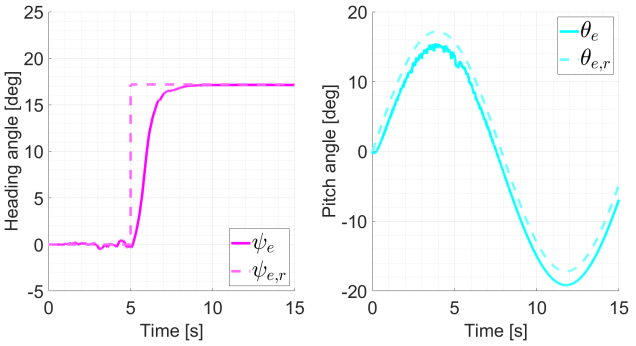

Figure 8: Simulated behaviour and references on heading and pitch of end-effector.

5.3 *Force input*

In this last simulation experiment, a step function of 1 N force was imposed in the X_I- and Z_I-directions on the end-effector to validate the response under contact force. The force input was given by step function.

In Figure 9, the inputs to the impedance layer (desired, $\boldsymbol{x}_{e,d}$) and outputs (reference, $\boldsymbol{x}_{e,r}$) of the impedance filter are given,along with the response of the system. The results shows that the impedance filter creates smooth, continuous references that the position controller can follow quite well.

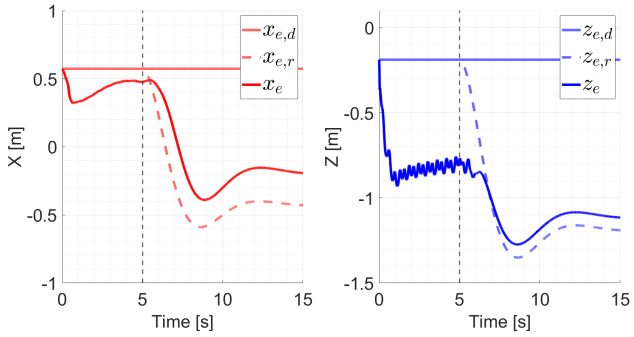

Figure 9: Simulated x- and z responses of impedance filter and system when force is applied as unit step at t = 5.0 s, indicated by dashed vertical line.

A steady-state error appears in the X_I direction because the position controller in this direction has no integral gain, so it will remain offset when a force is present. This offset will cause the drone body to lean into the wall during interaction and is therefore desirable and expected.

6 Flight Experiments

Flight experiments were carried out to demonstrate the effectiveness of the proposed manipulator and controller. The experimental setup is discussed first, with different experiment types discussed thereafter.

6.1 *Experimental setup*

The proposed manipulator is attached to a ProSkyTec HoverS quadrotor. This platform has a PX4 CUAV5+ as its flight controller and a Raspberry Pi 4 as its companion computer. The impedance filter and position inverse kinematics algorithm are implemented in ROS Melodic [21].

The manipulator uses potentiometers (rotary and linear) along with an Analog-Digital Converter (ADC) for position feedback. The active degree of freedom is powered by a Dynamixel XH430-W210-R, which is interfaced with ROS. A DC/DC converter is added to regulate voltage from the onboard 6S battery to the companion computer and Dynamixel.

The higher-level task planner was programmed via a Finite State Machine (FSM) that generates references for the desired end-effector pose, which are passed on to the impedance filter and subsequently to the lower layers of the control scheme. This way, the experiments can be carried out fully autonomously using preprogrammed conditions.

The experiments are carried out at TU Delft's Cyberzoo, a flight arena equipped with a motion capture system (Optitrack) to accurately provide position feedback on the drone. The motion feedback system streams the pose data to the companion computer through a wireless LAN, which in turn relays it to the flight controller using MAVROS.

The target surface for physical interaction is a wall which

can be rotated, enabling contact experiments over vertical and overhanging surfaces. The angle incline of the wall can be finely regulated via a scaled hinge that locks in place.

6.2 *Implementation validation*

To validate the ROS-based implementation of the different layers of the controller and to ensure the intended behaviour of the UAM before contact experiments were commenced, several free-flight experiments were done. The validation experiments are structured in a similar way to the simulation experiments: first an end-effector position tracking experiment was carried out, and secondly a end-effector orientation tracking experiment was done.

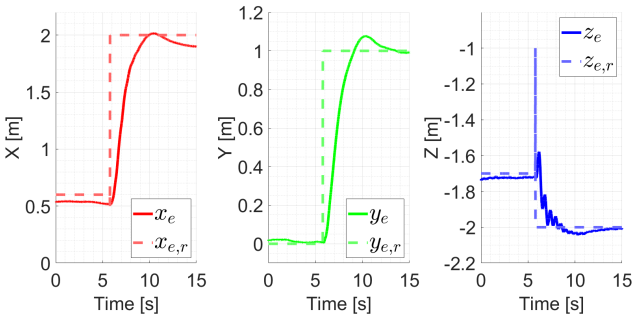

Figure 10: End-effector XYZ position in waypoint experiment.

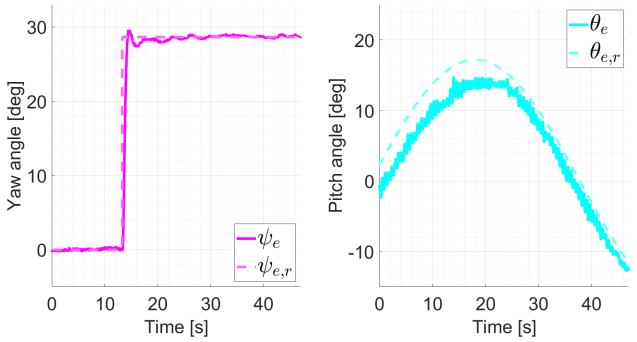

Figure 11: End-effector heading and pitch in orientation experiment.

Figure 10 shows the responses of the system to a step input on the end-effector position reference. Figure 11 shows the responses of the system to a step input on the end-effector heading (ψ_e) and a sinusoidal input on the end-effector pitch (θ_e). In both cases, the responses of the system show good convergence to the reference values, with some small oscillations on z_e in the waypoint experiment and a slight offset on the pitch during the end-effector orientation experiment. The oscillation on z_e can be attributed to a combination of excitation because of the reference 'spike' visible in the figure, along with the high inertia coming from the manipulator. The offset in θ_e is attributable to the relatively high mass and arm of the manipulator, causing a high holding torque on the servo to be needed to keep the arm in position.

6.3 *Vertical wall interaction*

The vertical wall experiments focuses on interaction without adding the overhang inclination. In this experiment, the UAM approaches the wall and establishes contact, maintains this contact for a time and disengages again. The experiment was repeated multiple times during a single flight. The impedance parameters are set as the identity matrix multiplied by a scaling factor for the mass- and stiffness matrices. The damping matrix was also set as the identity matrix, but the scaling factor here was calculated to be critical from the mass and stiffness scaling factors, see Table 2.

In addition to the vertical wall interaction results, Table 3 shows the mean maximum interaction force along with standard deviation of the maximum forces between the experiments, with the same data for the absolute yaw error during interaction. The highest interaction forces could be achieved on the vertical wall, while the interaction forces during the overhanging wall experiments are still quite substantial. The absolute yaw error is shown because undesired yawing of the drone during interaction was a major cause of failure during the experiments. Another major cause of failure during free-flight was a pitch oscillation of the drone, which was then compensated for with delay by the servo. This delay causes the manipulator to excite the pitch oscillation of the drone until the UAM destabilises completely.

Table 2: Parameters of the contact experiments.

Parameter	**value**
M_d scaling	1
K_d scaling	10
D_d scaling	$2\sqrt{M_d K_d}$
$v_{approach}$	0.05 m/s

The mean maximum forces in Table 3 are expressed as a percentage of the UAM's total mass for comparison to similar systems at a different scale, see Table 4.

A single sample of the vertical wall interaction experiments is shown in Figure 12. It shows the development of interaction force during the experiment, $\boldsymbol{x}_{e,d}$ and the resulting $\boldsymbol{x}_{e,r}$ coming from the combination of the interaction force and impedance filter. Lastly, the Euler angles of the drone and the q_1 angle are shown. The yaw angle fluctuates more heavily than the roll angle, which coincides with visual observations

Table 3: Mean (μ) and standard deviation (σ) of maximum force and maximum yaw error between the experiments.

Exp.	n_{exp}		**max**(F_{q2})	**max**($\psi_{b,err}$)
Vertical	11	μ	5.66 N	3.47°
		σ	0.67 N	1.21°
10°	14	μ	3.63 N	3.13°
		σ	0.54 N	1.41°
20°	11	μ	3.56 N	2.32°
		σ	0.32 N	0.73°
EE mod.	8	μ	2.80 N	3.57°
		σ	0.19 N	1.22°

Table 4: Average maximum forces as percentage of UAM weight for comparison across scales.

UAM total mass/weight			2.985 kg	29.28 N
Experiment:	Vertical	10°	20°	EE mod
max($F_{q2,\mu}$)	5.66 N	3.63 N	3.56 N	2.80 N
% of weight	19.3%	12.4%	12.2%	9.6%

and the main cause of failure during interaction, which was an undesirable yaw that can destabilise the system. Furthermore, q_1 roughly mirrors θ_b, which means the servo correctly compensates for θ_b to keep the end-effector in the same orientation.

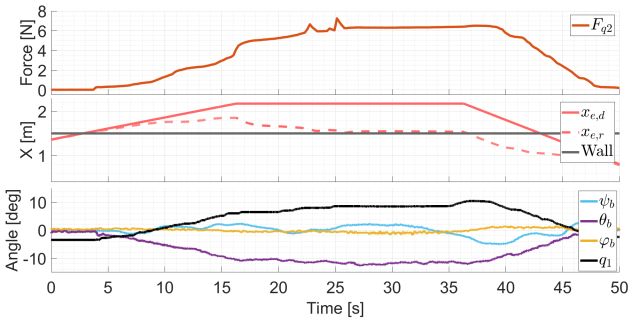

Figure 12: Single vertical wall experiment, plot with $x_{e,d}$ and $x_{e,r}$ is shown to demonstrate impedance filter.

In Figure 13 the mean, standard deviation and minimum/maximum force over the set of 11 experiments are shown. The bands around the mean are quite narrow indicating that the force profile over the different experiments is very similar.

Demonstrating the reliability and repeatability of the system, Figure 14 shows a sequence of 7 consecutive interactions during a single flight. Similar observations to the ones noted above can be made with regards to ψ_b, θ_b and q_1, although it should be noted that the experiment presented in Figure 12 is not part of the set presented in Figure 14, but from a different flight.

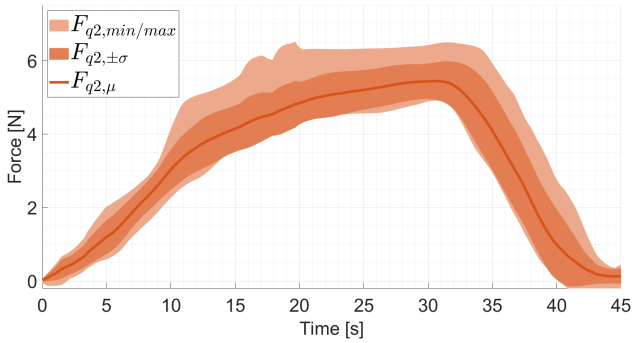

Figure 13: Aggregate results over series of 11 vertical wall experiments, showing the minimum and maximum, the standard deviation, and the mean of the recorded force.

6.4 *Overhanging wall interaction*

After successfully carrying out multiple vertical wall experiments, the overhang inclination angle of the wall was raised to 10° and 20°, respectively. Similar experiments were carried out with lower maximum forces and the impedance parameters of the vertical wall experiments were observed.

During the 10° inclination experiments (shown in Figure 15 and 16) similar observations were made as during the vertical wall experiments, with the undesirable effects setting in at lower interaction forces than with the vertical wall experiment. The initial q_1 is higher because the end-effector is positioned prior to interaction, but the compensatory behaviour with respect to θ_b is still clearly visible. Note that the high maximum force during the second half of the experiments as shown in Figure 16 is due to two experiments in the set that had slightly different settings causing the force during the holding phase of the experiment to be higher. This was found to reduce reliability and cause the UAM to destabilise faster.

The same observations can be made for the 20° overhang inclination experiments shown in Figure 17 and 18. The initial q_1 value is higher because of the prepositioning of the manipulator. Here too, ψ_b fluctuates more than φ_b, implying the lower stability of this state. This instability is partly caused by the force balance during interaction, but also by the substantially lower yaw authority that quadrotors inherently possess. The force can be regulated quite closely and repeatably as shown in Figure 18, apparent through the narrow mininum/maximum and standard deviation bands.

6.5 *End-effector modification*

Given that undesired yaw was a major cause of failure observed at high forces, several experiments were done with the end-effector configured at a 90 degree angle, such that

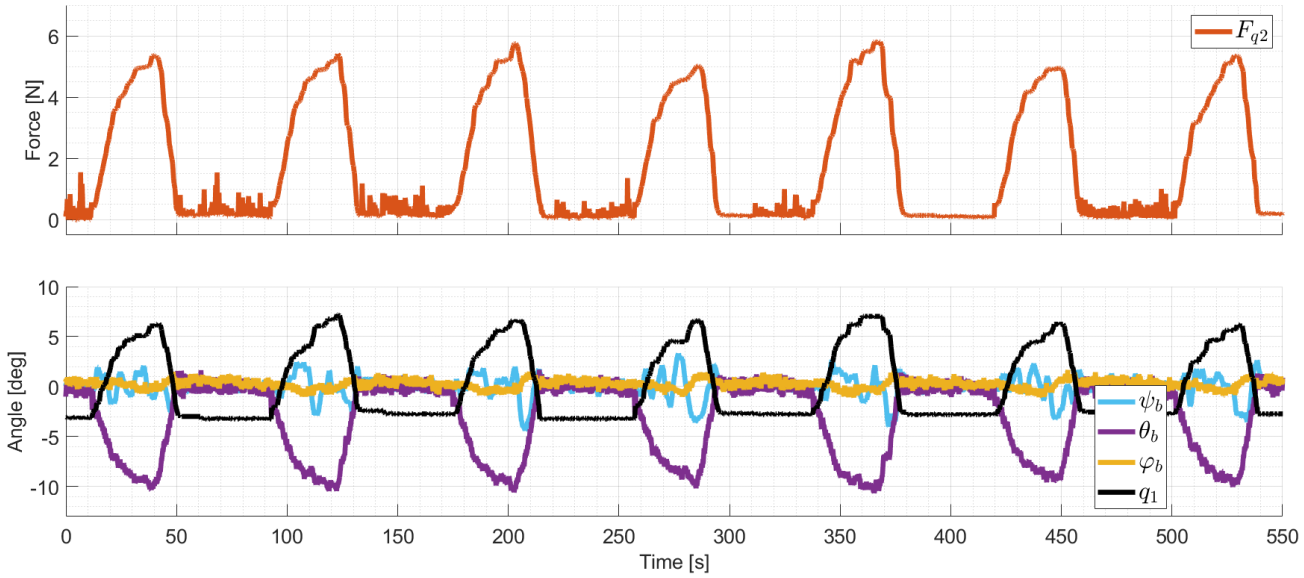

Figure 14: Interaction force and Euler angles of a sequence of seven experiments during single flight.

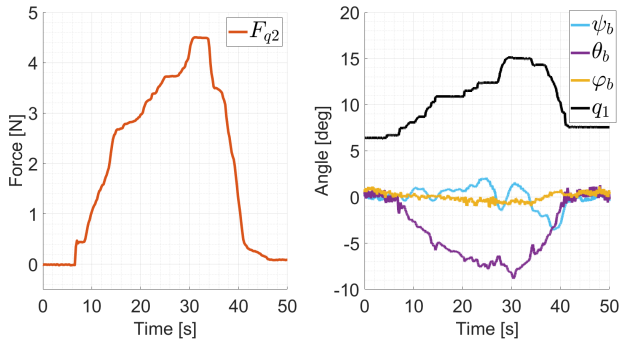

Figure 15: Force, Euler angles and q_1 during a single 10° overhang experiment.

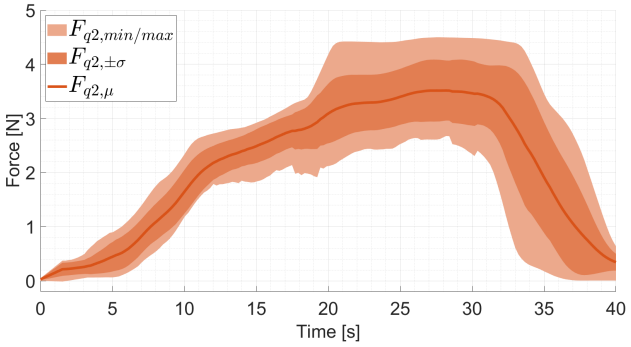

Figure 16: Aggregate results over series of 14 10° inclination experiments, showing the minimum and maximum, the standard deviation, and the mean of the recorded force.

q_3 decouples end-effector yaw from the drone's yaw angle. The experiments with this configuration were all done on a vertical wall with the same impedance parameters as before.

The interaction force for repeatable experiments (shown in Figure 20) was lower than in the other experiments, but this was mainly limited by the servo failing (and thus destabilising the UAM) at higher forces. This can be attributed to inaccuracy in the drone's altitude control. Small deviations in the drone's altitude cause high reaction torques on the servo due to external reaction forces lateral to the interaction surface. The servo has an overload protection shutting it down when the requested current becomes too high. Furthermore, in Figure 19 it can be seen that q_3 follows ψ_b in the second half of the experiment, suggesting it compensates somewhat for the yaw error of the drone. In this figure we can also clearly see how q_3 is complying to the yaw angle of the wall in the inertial frame when contact is established.

6.6 *Impact*

Finally, the robustness of the system to impact was assessed. The UAM was moved several meters away from the wall, and would approach at a preset velocity. When the impact is registered, the UAM attempts to regain stabilisation in free-flight. During this experiment the pitch compensation term in the inverse kinematics was disabled to omit the pitch oscillations causing destabilisation during free-flight.

Experiments were carried out at 0.5, 1.0 and 1.5 m/s of approach speed, but 1.5 m/s was found to be too high of a speed for the UAM to handle. Slow reading of q_2 was

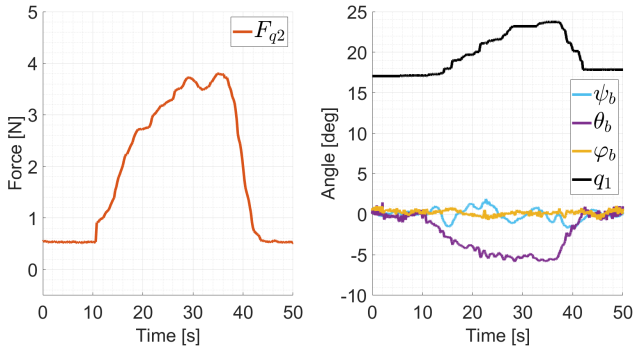

Figure 17: Force, Euler angles and q_1 during a single 20° overhang experiment.

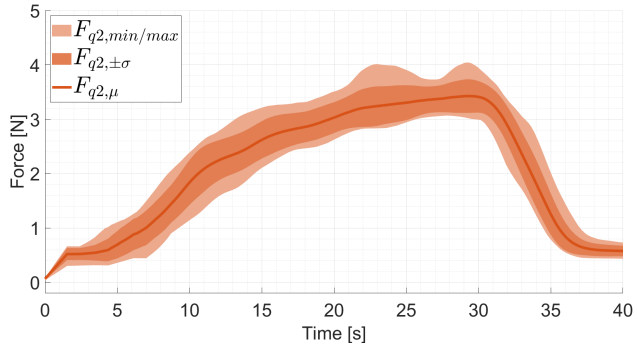

Figure 18: Aggregate results over series of 11 20° inclination experiments, showing the minimum and maximum, the standard deviation, and the mean of the recorded force.

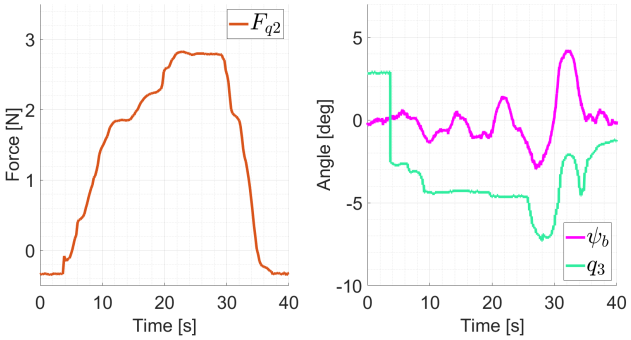

Figure 19: Single example of the vertical wall experiment with end-effector modification.

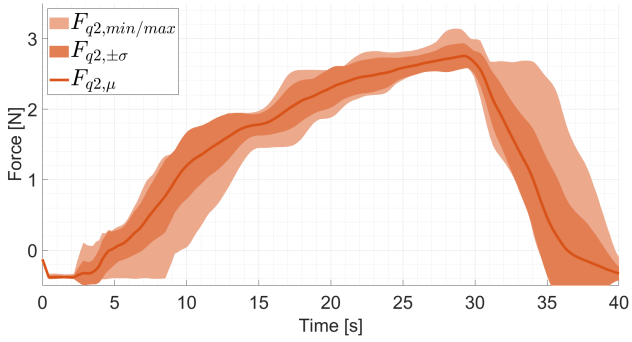

Figure 20: Aggregate results over series of 8 end-effector modification experiments, showing the minimum and maximum, the standard deviation, and the mean of the recorded force.

problematic for an interaction this dynamic, as at higher speeds the collision was detected quite late so corrective action of the UAM was also delayed. Investigation of node speeds show that the ADC could be read at a maximum of 4.78 Hz (with a target frequency of 50 Hz), explaining this delay.

A successful experiment at 1.0 m/s is shown in Figure 21. The maximum force recorded is at 16 N, which is also the force corresponding to maximum travel of q_2, further supporting the finding that a velocity of 1.5 m/s is outside of the system capacity. A strong oscillation in pitch was observed, but could be corrected through the drone's pitch controller.

7 Conclusion

In this work a detailed and applied example of centralised modeling for aerial manipulators was presented, which may help others looking to apply this theory to aerial manipulation systems of differing morphologies. A centralised impedance control scheme was implemented to complement the physical compliance of the proposed manipulator design. The approach was validated in simulation and has been shown to robustly and reliably handle the transition between free-flight and contact, while providing embedded force feedback and allowing relatively high interaction forces of up to 19.3% of the UAM weight.

Experiments were done on vertical walls and walls with overhang angles up to 20°, which could all be handled through decoupling of the platform pitch angle and end-effector pitch angle through the servo. The major failure modes with this particular system were identified as a pitch oscillation originating from the pitch compensation term in the position inverse kinematics combined with the hardware limitations of the servo (occurring during free-flight) and an undesirable yawing about the interaction point at high forces when in contact.

Through the presented experiments, this work shows that intelligent design can help tackle multiple problems at once, providing robustness and versatility to aerial manipulation systems.

Further work building on this project can look into simulation modelling and hardware improvements.

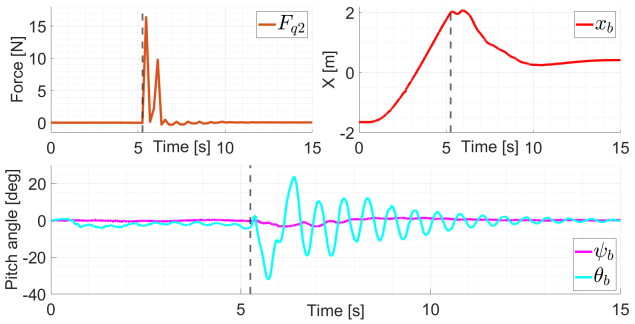

Figure 21: Impact test at 1.0 m/s with moment of impact indicated by vertical black dashed line, showing stabilisation after impact.

The simulation's fidelity can be increased when a software-in-the-loop (SITL) or hardware-in-the-loop (HITL) implementation is done for the position controller, as this provides very accurate simulation of the real flight controller. Adding contact dynamics starting by a simple admittance of high stiffness helps to demonstrate and tune the impedance characteristics for specific missions.

With regards to the hardware, the end-effector design was left out of the scope of this work, but it becomes essential for accomplishing specific contact-based tasks. Further work also includes tackling the main causes of failure that were observed, i.e. the undesired yawing about the interaction point during contact, and the undesired pitch oscillation originating from hardware limitations and the pitch compensation part of the inverse kinematics layer.

For pitch oscillations experienced at the servo motor, the recommendation is the integration of a more performing actuator with higher frequency, to reduce latency between the low-level controller and the commanded motor output following the inverse kinematics computation.

Further behaviours on the compliant aerial manipulator could be implemented, such as pulling motion to retrieve an object from a surface. Lastly, higher level perception and autonomy in the form of vision or proximity sensing would further automate the operations, minimising human input in uncertain conditions.

References

[1] F. Ruggiero, V. Lippiello, and A. Ollero. Aerial manipulation: A literature review. *IEEE Robotics and Automation Letters*, 3(3):1957–1964, 2018. doi: 10.1109/LRA.2018.2808541.

[2] A. Ollero, M. Tognon, A. Suarez, D. Lee, and A. Franchi. Past, present, and future of aerial robotic manipulators. *IEEE Transactions on Robotics*, 38(1):626–645, 2021. doi: 10.1109/TRO.2021.3084395.

[3] J. Yick, B. Mukherjee, and D. Ghosal. Wireless sensor network survey. *Computer networks*, 52(12):2292–2330, 2008. doi: 10.1016/j.comnet.2008.04.002.

[4] S. Hamaza, A. Farinha, H. Nguyen, and M. Kovac. Sensor delivery in forests with aerial robots: A new paradigm for environmental monitoring. In *2020 IEEE/RSJ International Conference on Intelligent Robots and Systems (IROS): Workshop on Perception, Planning and Mobility in Forestry Robotics (WPPMFR 2020)*, 2020.

[5] S.H. Mathisen, V. Grindheim, and T.A. Johansen. Approach methods for autonomous precision aerial drop from a small unmanned aerial vehicle. *IFAC-PapersOnLine*, 50(1):3566–3573, 2017. doi: 10.1013/j.facol.2017.08.624.

[6] S. Hamaza, I. Georgilas, M. Fernandez, P. Sanchez, T. Richardson, G. Heredia, and A. Ollero. Sensor installation and retrieval operations using an unmanned aerial manipulator. *IEEE Robotics and Automation Letters*, 4(3):2793–2800, 2019. doi: 10.1109/LRA.2019.2918448.

[7] D.R. McArthur, A.B. Chowdhury, and D.J. Cappelleri. Autonomous control of the interacting-boomcopter uav for remote sensor mounting. In *2018 IEEE International Conference on Robotics and Automation (ICRA)*, pages 5219–5224. IEEE, 2018. doi: 10.1109/ICRA.2018.8461119.

[8] D. Zhang, R. Watson, G. Dobie, C. MacLeod, and G. Pierce. Autonomous ultrasonic inspection using unmanned aerial vehicle. In *2018 IEEE International Ultrasonics Symposium (IUS)*, pages 1–4. IEEE, 2018. doi: 10.1109/ULTSYM.2018.8579727.

[9] T. Ikeda, S. Yasui, M. Fujihara, K. Ohara, S. Ashizawa, K. Ichikawa, A. Okino, T. Oomichi, and T. Fukuda. Wall contact by octo-rotor uav with one dof manipulator for bridge inspection. In *2017 IEEE/RSJ International Conference on Intelligent Robots and Systems (IROS)*, pages 5122–5127, 2017. doi: 10.1109/IROS.2017.8206398.

[10] H.W. Wopereis, J.J. Hoekstra, T.H. Post, G.A. Folkertsma, S. Stramigioli, and M. Fumagalli. Application of substantial and sustained force to vertical surfaces using a quadrotor. In *2017 IEEE International Conference on Robotics and Automation (ICRA)*, pages 2704–2709, 2017. doi: 10.1109/ICRA.2017.7989314.

[11] V. Lippiello and F. Ruggiero. Cartesian impedance control of a uav with a robotic arm. *IFAC Proceedings Volumes*, 45(22):704–709, 2012. doi: 10.3182/20120905-3-HR-2030.00158.

[12] G. Arleo, F. Caccavale, G. Muscio, and F. Pierri. Control of quadrotor aerial vehicles equipped with a robotic arm. In *21St mediterranean conference on control and automation*, pages 1174–1180. IEEE, 2013. doi: 10.1109/MED.2013.6608869.

[13] E. Cataldi, G. Muscio, M.A. Trujillo, Y. Rodríguez, F. Pierri, G. Antonelli, F. Caccavale, A. Viguria, S. Chiaverini, and A. Ollero. Impedance control of an aerial-manipulator: Preliminary results. In *2016 IEEE/RSJ International Conference on Intelligent Robots and Systems (IROS)*, pages 3848–3853. IEEE, 2016. doi: 10.1109/IROS.2016.7759566.

[14] K. Bodie, M. Brunner, M. Pantic, S. Walser, P. Pfändler, U. Angst, R. Siegwart, and J. Nieto. An omnidirectional aerial manipulation platform for contact-based inspection. *arXiv preprint arXiv:1905.03502*, 2019. doi: 10.15607/RSS.2019.XV.019.

[15] M. Ryll, G. Muscio, F. Pierri, E. Cataldi, G. Antonelli, F. Caccavale, D. Bicego, and A. Franchi. 6d interaction control with aerial robots: The flying end-effector paradigm. *The International Journal of Robotics Research*, 38(9):1045–1062, 2019. doi: 10.1177/0278364919856694.

[16] A. Suarez, G. Heredia, and A. Ollero. Lightweight compliant arm for aerial manipulation. In *2015 IEEE/RSJ International Conference on Intelligent Robots and Systems (IROS)*, pages 1627–1632. IEEE, 2015. doi: 10.1109/IROS.2015.7353585.

[17] A. Suarez, G. Heredia, and A. Ollero. Physical-virtual impedance control in ultralightweight and compliant dual-arm aerial manipulators. *IEEE Robotics and Automation Letters*, 3(3):2553–2560, 2018. doi: 10.1109/LRA.2018.2809964.

[18] B. Siciliano, O. Khatib, and T. Kröger. *Springer handbook of robotics*, volume 200. Springer, 2008. ISBN: 978-3-540-23957-4.

[19] B. Siciliano, L. Sciavicco, L. Villani, and G. Oriolo. *Robotics: Modelling, planning and control*. Springer-Verlag London (UK), 2009. doi: 10.1007/978-1-84628-642-1.

[20] R. Tedrake. *Underactuated Robotics: Algorithms for Walking, Running, Swimming, Flying, and Manipulation*. 2022. URL `https://underactuated.csail.mit.edu`. Course Notes for MIT 6.832.

[21] Stanford Artificial Intelligence Laboratory et al. Robotic operating system. URL `https://www.ros.org`.

Part II

Literature study

Assessed January 2022 for AE4020: Literature Study

List of Figures

List of Tables

2

Introduction

Unmanned Aerial Vehicles (UAVs) are a versatile subclass of unmanned vehicles which can fly, providing them with virtually unlimited reach, only limited by endurance. While different types such as rigid wing UAVs, helicopter UAVs and lighter-than-air UAVs exists, by far the most well-known is the conventional quadcopter or drone.
UAVs also have widespread uses in industry, and they are mainly deployed as platforms for visual inspection of industrial plants, oil & gas pipelines, mapping & surveying of terrain, search & rescue operations and environmental monitoring. These tasks all utilise the UAV as a platform for remote sensing tools. The avoidance of physical interaction with the environment characterises current and past use of UAVs [1].

Since about two decades, researchers have attempted to break this paradigm with increasing amounts of success by designing and testing unmanned aerial manipulators (UAMs). UAMs are a combined system of flying platform and robotic manipulation system, allowing physical manipulation and interaction with the workspace of a UAV. The potential for aerial manipulation is huge: expanded with the ability to grasp, perch and manipulate, the possible operations increase substantially. In the future many routine maintenance operations in hazardous locations can be automated, reducing required time, economic cost and risk to the human workers involved [2]. For example, UAMs can be employed to carry out work in hazardous and inhospitable environments, such as in chemical or nuclear plants, or at height such as in the (offshore) wind power industry. Driven by these potential gains, there has been a lot of interest in this topic, both from industry and from policy makers. Following this interest, there has been tremendous growth in the field. Starting from rudimentary interaction experiments [3], impressive demonstrations of the possibilities have been given recently: valve turning [4], haptic inspection [5] and pick-and-place [6] have been shown to be possible using aerial robots.

This work focuses on the placement and retrieval of small sensor payloads. This application is becoming more relevant as visions of 'smart cities' include large-scale data harvesting by the deployment of wireless sensor networks. This technology is in turn enabled by the increasing commercial availability of Internet of Things (IoT) ecosystems, which allow parties to develop and deploy sensors with connectivity to extract data regularly. Examples of use cases for these wireless sensor networks are structural health monitoring in buildings or civil works such as bridges or dams, or deployment of air quality sensors in densely populated areas to assess health risks.

The act of placing and retrieving a sensor payload is generalised to the task of controlled force application, where a UAM needs to use its end-effector to exchange a force with its environment without destabilising. The problem of sensor placement is equal to that of force exertion from a system design and control perspective, and mainly differs in end-effector design (and not much else) from a mechanical perspective. Furthermore, it allows the research to translate better to other operations such as contact-based inspection [7], where UAMs can add considerable benefits.

This literature study presents an overview of relevant research to the task of force application by UAM. Chapter 3 goes deeper into the topic and explains the structuring of the main body of the document. This

main body consists of the three features that the system has been divided into, which are the aerial platform (discussed in chapter 4), the manipulation system (discussed in chapter 5) and the control system (discussed in chapter 6). At the end, the conclusion summarises the main points of these chapters and reiterates the choices made based on the knowledge presented in the other chapters. The conclusion is presented in chapter 7.

2.1. Research plan

In this section, the research plan is presented. Starting with the motivation behind this work, it zooms in on the research question and sub-questions to be answered by this project. It concludes with the research objective, which is divided into sub-objectives that should be completed during the project.

2.1.1. Research aim (motivation)

The aim of this research is the development of a UAM with the capability to place sensors on horizontal, vertical and inclined (overhanged) surfaces. This operation can be generalised to the application of a controlled force on the surface, as sensors in this context can be placed by means of an adhesive tape which requires a substantial normal force to be applied. Ideally the applied force can be in tension and compression (pushing and pulling motion) to retrieve sensors when they have concluded their useful life or need maintenance (for example a battery swap). The aim of this research is also to enable these operations from a conventional quadrotor platform, because of the ubiquity of these vehicles. The dynamics, control and behaviour of underactuated aerial platforms has been extensively researched and commercialised, meaning there is a lot of knowledge about these platforms and they are relatively economical to deploy.

The main challenges are the design of an integrated system of platform, manipulator and controller that allows such a large workspace while maintaining accuracy and mechanical compliance, and that can handle large external forces and exploit the aerial platform's attitude to regulate and enhance applied forces. The large workspace is necessary to adapt to different environmental geometries. The accuracy is needed to guarantee placement in the correct position and the mechanical compliance is needed to deal with the transition from free-flight to contact and to counteract disturbance propagation from the platform to manipulator and vice versa.

2.1.2. Research question

The main research question that this thesis project aims to answer is:

> **"How can the workspace, magnitude and accuracy of force applied from an underactuated aerial platform be improved compared to the current state of the art?"**

This research question is divided into a number of sub-questions, which break down the main question into more workable components. Answering the sub-questions will lead to insights allowing the formulation of a definite answer to main question. The sub-questions are listed below.

- What manipulation system design allows for a larger workspace and higher accuracy?
  - Can compliance be incorporated on available degrees of freedom (DoF)?
  - Is a parallel or serial robot better suited for this application?
  - Can disturbances and inaccuracies on the aerial platform be rejected by the manipulation system?
- How can the control system deal with substantial external forces?
  - What is the maximum exerted force of the system as ratio of its mass?
  - Is computational power on mobile platforms sufficient for the required control system?
  - How to deal with the nonlinearity at attitudes?
- How can a tangential position and normal force references be tracked accurately?
  - Is a decoupled control system capable of reaching high accuracy?
  - How to accurately determine the end-effector's position with respect to the environment?

- Should direct force feedback be included or is indirect force feedback sufficient?

While the three main themes of this research (workspace, accuracy and magnitude) are loosely related to the three sub-questions mentioned here, they are highly interrelated as can be seen from the second level of questions. For some of the questions it will be possible to answer with high degree of certainty by reviewing the literature presented in this report, but for some of the questions it will be necessary to analyse the results from the experiments that are planned for a later stage of the project. It should be noted that the research questions remain in development and can hardly be fixed as it is very hard to predict the specific issues that are going to arise when the project advances.

2.1.3. Research objective

The goal of the research project is described by the research objective. By answering the proposed research question and sub-questions, the following research objective is achieved:

> **"To achieve substantial force application in a large workspace with high position and force tracking accuracy from a quadrotor platform to enable sensor placement on surfaces of different orientations by design of a manipulation system and coupled control logic."**

In order to achieve the research objective as described above, a number of sub-objective also needs to be achieved. The research project will start with a precise problem definition in mathematical terms, that can be used in later stages to design a model and appropriate controller for the system. Next, the manipulator's physical design needs to be determined. This means establishing on the component level which parts are needed and how they will fit together, along with sourcing the parts. Simultaneously, the design of the control algorithms can be refined until eventually completed. A system model needs to be established which can be used to tune the controller and verify its efficacy. With the physical system and its software ready, it should be ensured that the software runs well on the physical system hardware and that the setup behaves as expected. This is mostly done using simulations, which will not only allow for testing of the software but also for modelling the UAM's behaviour in the real world.

When the control software is verified, experimental data can be gathered in a number of lab setups. Optionally to increase confidence in the success of the setup, indoor and outdoor experiments could also be run to demonstrate disturbance rejection capabilities and provide a more realistic scenario. Finally, the resulting data needs to be processed and documented accordingly, at which point the main objective is shown to be completed, or the necessary follow-up work can be identified.

It should be noted that while the sub-objectives are presented here in a sequential manner, the execution will most likely follow a more iterative approach. It is expected that during preparation and execution of the experiments discoveries will be made about the system that will prompt changes to be made to the initial idea. This is a learning process, and as such it is impossible to accurately and definitively predict the entire process. While they may change over the course of the research project, the objective and sub-objectives presented above provide a good initial framework for the work to be done.

3

Aerial Manipulation

Aerial manipulation is a relatively new field of research that looks at manipulation tasks using robotic tools that are placed on an aerial platform or UAV. In this chapter, a top level overview will be given of the field. At first, definitions of reference frames, pose and wrench are established in section 3.1. Afterwards, section 3.2 will introduce aerial manipulation as a field and split the UAM up into its three constituent parts. Section 3.3 discuss typical tasks that UAMs aim to complete and tasks that are still left for further research. Finally, section 3.4 presents a short summary of this chapter.

3.1. Definitions

Before starting the discussion on aerial manipulation, it is useful to define the most important reference frames used in this work and other research. Additionally, the concepts of pose and wrench are discussed as they are fundamental to the study of (aerial) robotics.

3.1.1. Reference frames

In general, the reference frames defined by Mulder *et al.* [8] will be used as a baseline for the reference frames of this work, with some alterations to suit them better to the study of UAMs given that the original definitions are set up for fixed-wing aircraft.

The main assumption is that the world consists of a single flat, infinite plane. This greatly simplifies equations of motion and in general the conceptualisation of the aerial manipulation task. It was deemed appropriate since on the spatial scales that are of interest to UAMs the curvature and rotation of the Earth is irrelevant.

The reference frames defined here are the most important ones necessary for discussions on aerial manipulation. They are all right-handed orthogonal axis systems and the origin and directions of the axes are described below. Additionally, figure 3.1 shows a graphical depiction of the reference frames for better visual understanding.

- **Inertial reference frame** F_I: a non-moving reference frame fixed to an arbitrary point on the ground. The $X_I Y_I$-plane is tangent with the ground with the X_I axis fixed in an arbitrary direction. The Z_I axis points up.
- **Body-fixed reference frame** F_b: reference frame fixed at the vehicle's center of gravity (CoG) with the X_b axis pointing forwards. The Y_b axis points to the right of the vehicle. This frame rotates with the vehicle body.
- **Vehicle-carried normal Earth reference frame** F_E: reference frame fixed at the vehicle's CoG with the $X_E Y_E$-plane parallel to the world's surface, with the Z_E-axis pointing down with the gravity vector. The X_E axis points north and the Y_E axis pointing east. The X_E and Y_E axes align with the X_b and Y_b when the vehicle is in perfect hover with zero heading angle.
- **End-effector reference frame** F_M: reference frame fixed to the end-effector. Generally, the Z_M axis points away from the end-effector with the $X_M Y_M$-plane orthogonal to that, but the specific definition depends on the end-effector design.

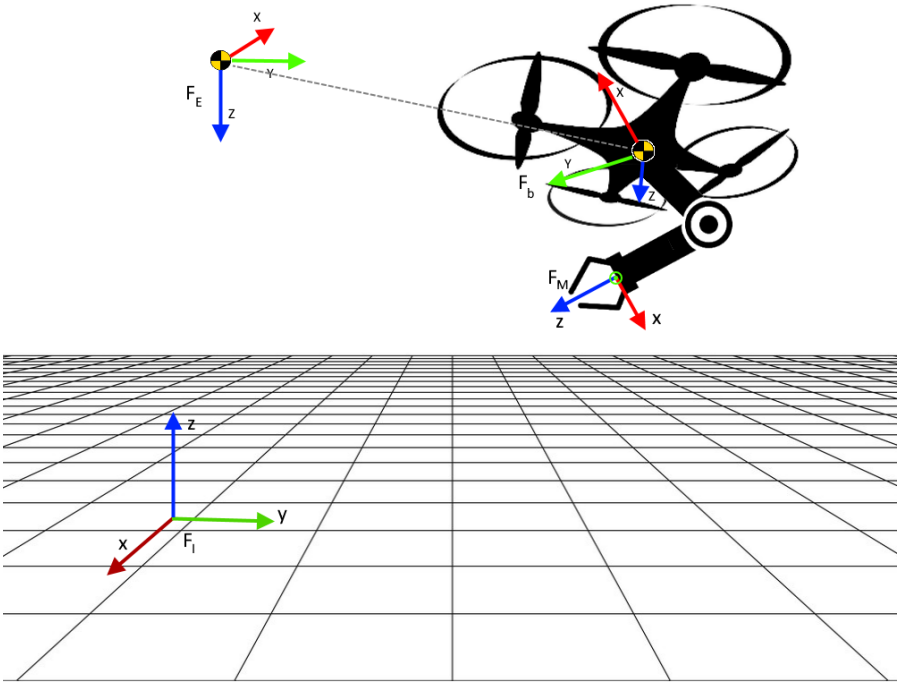

Figure 3.1: Graphical representation of the most important reference frames for aerial manipulation (own work)

3.1.2. Pose and wrench

Before the constituent parts of the aerial manipulator can be discussed, it is useful to define the notion of *pose* and *wrench*, two fundamental concepts in (aerial) robotics.

Pose $\vec{p} \in \mathbb{R}^6$ refers to the combination of position and orientation of the aerial platform or manipulator. It is a six-dimensional real vector fully describing the components related to the position and orientation of the agent in real space. In principle, the pose and wrench of any reference frame with respect to any other can be given. In this work, the pose will be defined as a vector consisting of the three xyz-position coordinates (strictly the location of the origin of F_b w.r.t. F_I) and the three Euler angles of F_b w.r.t. F_E. A mathematical description of pose and wrench is given below.

$$\vec{p} = \begin{bmatrix} x & y & z & \theta & \phi & \psi \end{bmatrix}^T \qquad \vec{w} = \begin{bmatrix} \sum F_x & \sum F_y & \sum F_z & \sum M_x & \sum M_y & \sum M_z \end{bmatrix}^T$$

Wrench $\vec{w} \in \mathbb{R}^6$ is the force/moment equivalent of the pose. The wrench is the six-dimensional real vector describing all components related to forces and moments acting on a body. It starts with the three forces in X, Y, and Z direction of the reference frame in which the wrench is expressed (denoted with a subscript, like $\vec{w}_b$ for the wrench on the origin of F_b). The other three elements are the moments about the axes in the same order, following the right-hand rule. Because the wrench is expressed as a single vector containing all forces and moments about the origin of a reference frame (or any arbitrary other point), the forces and moments need to be summed about this point.
The position and orientation of a robotic manipulator can also be described using the generalised coordinates $\vec{q}$. These represent the configuration of the system relative to a reference. In the context of robotics, the terms of q often refer to the joint angles (where an arbitrary angle for each joint can be defined as $0°$).

3.2. Unmanned Aerial Manipulators

In the last couple of years, the study of (unmanned) aerial manipulators (UAMs) has been established as a separate research field by the successive publication of a number of literature surveys [9, 1, 10, 11, 12, 2] and a comprehensive book [13]. These endeavours to structure and categorise works in the field

indicates that the technology is maturing and real-world applications are becoming more widespread.

While these works are not all structured in the same way, a general framework for UAMs can be established. Looking at a typical UAM (example provided in figure 3.2 [14]), a clear distinction exists between the aerial platform (also called unmanned aerial vehicle, UAV or simply drone) and the manipulation system. Aside from appearance, these systems also have a clear distinction in function: the aerial platform's function is to move the manipulator through the environment, while the manipulation system's function is to complete the tasks for which the UAM was designed.

Aside from the aerial platform and manipulator, the control system is defined as the third feature. The control system is comprised of the software generating the commands for the platform and manipulation system's acuatators. It is considered separate from the platform and manipulation system because of the system's scope and because the type of control system used is not (fully) dependent on the platform or manipulation system.

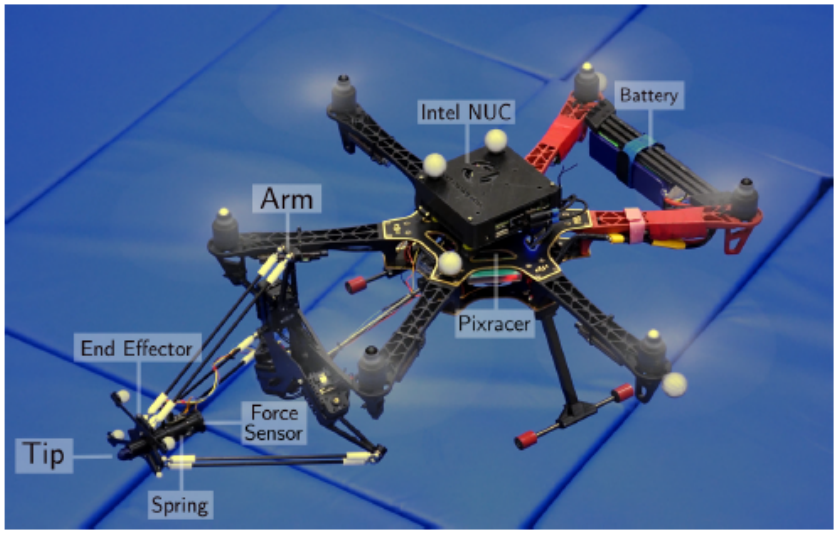

Figure 3.2: Example of a UAM used for aerial writing: the manipulator and platform are clearly distinguishable as the manipulator is mounted at the front of the platform and components are indicated (taken from [14]).

3.2.1. Aerial platform

The aerial platform or simply platform is a term used to refer to the vehicle subsystem of the aerial manipulator that carries the payload to the work location. This gives the aerial manipulator its virtually unbounded workspace because it allows the system to propel itself to anywhere in space provided that it is within endurance range, in Earth's lower atmosphere and within telecommunications range (unless fully autonomous).

The choice of aerial platform is integral to the design of an aerial manipulation system, as its dynamics and limitations provide a baseline for the capabilities of the manipulation system. For the conventional quadcopter, an important constraint is the underactuation of the platform. An underactuated platform is one which cannot independently control all wrench components. More information on underactuation is presented in section 4.3.2.

To deal with this coupling, some works use the DoFs of the manipulator to decouple the end-effector attitude/position from the platform attitude/position [15], whereas other works use a fully actuated platform to limit the need for decoupling the end-effector from the platform [16, 17].

Another limitation imposed by the aerial platform is that of relatively slow position tracking. Complex aerodynamic interactions between the rotors and the environment along with gust disturbances pose a challenge in control and stability, therefore performance and safety. An example of such a phenomenon is the ceiling effect [18], a similar effect to the ground effect where rotorcraft are pulled towards a

ceiling due to the low-pressure area they create between the vehicle and stationary wall. This type of phenomena causes the need for constant adjustment, decreasing pose tracking accuracy. Using the manipulator's DoFs to achieve higher positioning accuracy was demonstrated by performing the task of aerial writing [14].

3.2.2. Manipulation systems

Theory about the manipulation system mostly stems from the discipline of robotics, and is discussed more extensively in chapter 5. This section merely serves as an introduction to manipulation systems in the context of aerial manipulation.

The choice of manipulation system depends heavily on the task at hand. Task-specific manipulators can be kept simple, reducing the amount of DoFs and therefore enabling a less complex mechanical design and control system. As an example, Hamaza *et al.* [19] present a simple 1-DoF manipulator to enable sensor installation and retrieval with an underactuated platform. Going even further, in [16] and [17] the manipulators are rigidly attached to the platform, which needs to be fully actuated to comply with their requirements for force exertion on the environment. On the other hand, UAMs with higher numbers of DoFs are also possible. A fully redundant, 7-DoF KUKA robot arm was mounted to a unmanned helicopter in [20], highlighting the design freedom and possibilities in terms of DoFs.

3.2.3. Control of aerial manipulators

The most important concept introduced in the control of aerial manipulators is that of coupled or decoupled control. Given that the aerial platform and manipulation system can in essence be regarded as two separate systems, a control strategy can be devised for both systems, controlling for example their pose. In this case, the platform could be commanded to move to a certain location and the manipulator could be commanded at that location to carry out the task. However, when disturbances come into play this creates a difficult situation. The aerial platform will attempt to correct the disturbance, but in doing so will propagate other disturbances to the manipulator. Because their control systems are decoupled, the control system attempts to reject the error, but the moving masses of the manipulator create a disturbance for the platform to reject. This cycle enlarges the tracking error of the combined system. Several works have shown that this may create an unstable interaction [20], but this isn't necessarily true for all cases. A schematic representation of the decoupled control system is given in figure 3.3.

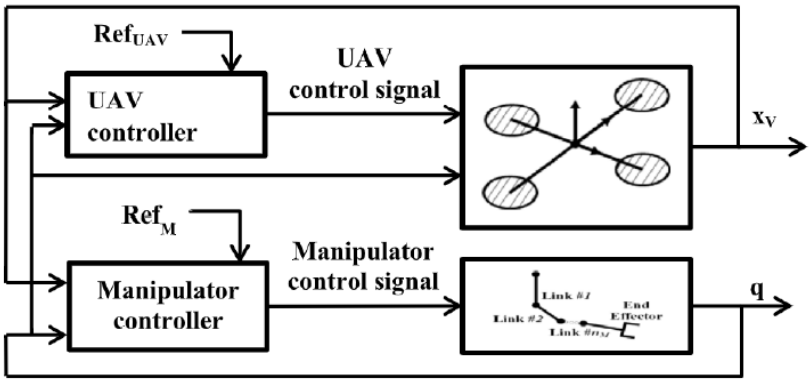

Figure 3.3: Block diagram of a decoupled control system, the control systems of the manipulator and platform are controlled separately. x_v denotes the platform state (taken from [1]).

The current trend is to move towards coupled control systems, that take into account the dynamics of the combined system to optimise actuation on all DoFs to minimise tracking error. This allows the system to use the manipulation system to compensate for position tracking errors on the aerial platform. Generally, the use of a coupled control system greatly improves tracking performance, but the drawback is that the combined model that needs to be derived is more complex and the control laws subsequently also become more complex. A schematic representation of the coupled control system is given in figure 3.4.

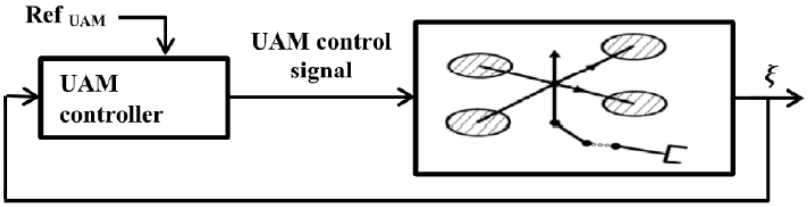

Figure 3.4: Block diagram of a coupled control system, the controller determines commands for both subsystems together. ξ denotes the UAM state (taken from [1]).

3.3. Aerial manipulation tasks

The systems described in this work are still in the research stage, but many of them have been designed to complete a certain task. This is usually done to either present an argument that a certain aerial manipulation task is possible or to demonstrate a certain property of the UAM that is accentuated by the task. In this section a brief overview of the different types of tasks is given.

3.3.1. Uncontrolled pose tasks

The first category is comprised of aerial manipulation tasks that do not require any (accurate) control over the pose of the manipulated object. These were among the first problems tackled by aerial manipulation, mainly by works investigating slung load transportation [21]. These tasks are then also not motion-constrained by their environment, as mentioned in the task taxonomy of Meng, He and Han [12]. This type of task does still pose the challenge of stability under a changing and possibly moving load causing disturbances on the aerial platform.

A more advanced case was presented by Papachristos, Alexis and Tzes [22]. They demonstrated that pushing/pulling objects could be an efficient way of handling heavy payloads that do not need to traverse large distances. In this work, no explicit control of the pose of the object or the exchanged force is presented, but the task that is demonstrated is more complex due to the higher forces between platform and object involved.

3.3.2. Controlled pose tasks

The next category of tasks comprises those that require pose control of the manipulated object, with increasing accuracy as technology developed. In this category, the flying hand as described by Ruggiero, Lippiello and Ollero [9], where the manipulated object is not able to move with respect to the platform. The platform in this case provides the object's pose control. These types of applications appeared quite early, but largely after the uncontrolled pose tasks. An example is aerial grasping from a helicopter by Pounds, Bersak and Dollar [23].

Other applications include construction work by aerial vehicles, as demonstrated by Augugliaro *et al.* [24]. In other work, the use of aerial vehicles as a 3D-printer head with unlimited workspace was explored [25].

3.3.3. Controlled wrench tasks

When tasks become motion-constrained [12], forces are exchanged with the environment. This class of tasks presents higher degrees of disturbances transferred to the platform, and is therefore more complex to handle. Early works on this tasks were performed by Albers *et al.* [3], where a quadrotor was modified with a support beam, extra propellor oriented towards the vertical wall and brush for cleaning windows and walls, although other potential use cases were named as well. More advanced force exchange tasks were investigated by Scholten *et al.* [26]. Accurate force control with relatively high force (40% of UAM weight) was shown through the use of a 7-DoF parallel manipulator, but only

in the positive direction (compression).

It was shown that passive [27] and active [28] compliance can be used to successfully manage the transition from free-flight to contact. The application of substantial (that is in the same order of magnitude as the UAM's weight) forces was found to be investigated by Wopereis *et al.* [15]. Negative forces and force trajectory tracking were shown in the context of sensor retrieval [19]. Force trajectory tracking in the context of pressing an emergency switch button was demonstrated with direct force feedback using a force sensor in the end-effector [29], but given the relative poor availability, quality and price of such sensors, a similar study was done using a force-sensorless approach, showing promising results [30].

Typical applications of force exertion are as shown before, the placing and retrieval of sensors, which as also investigated by McArthur, Chowdhury and Cappelleri [31], with less emphasis on the exchanged force. Additionally, contact inspection of infrastructure was discussed in detail by Ikeda *et al.* [5, 32]. In this work, forces were exerted both in the horizontal plane and upwards for bridge inspections.

3.3.4. Hybrid tasks

The combination of the above-mentioned pose- and force controlled tasks is presented as the fourth category of aerial manipulation tasks. In this motion-constrained type of tasks, one or more components of the pose need to be controlled while simultaneously the complementary wrench components need to be controlled. A first, preliminary work without explicit manipulator was carried out by Bellens, De Schutter and Bruyninckx [33].

A more recent work by Tzoumanikas *et al.* demonstrated aerial writing, where low-magnitude force references of 0.5 N were followed along with accurate position tracking (enhanced by the faster dynamics of the manipulator). A similar work which allows for more complex and accurate force trajectory tracking at higher magnitudes is identified as a next step in research.

3.4. Summary

In this chapter an introduction and overview of the field of aerial manipulation was given. The most important reference frames (inertial, body-fixed, vehicle-carried normal Earth and end-effector) were defined and pose and wrench were discussed as fundamental concepts in the study of aerial robotics. Thereafter the UAM was split up into three parts that can to some extend be analysed independently. The parts were the aerial platform propelling the system through the environment, the manipulation system which carries out the operation and the control system that takes in sensory data and creates the appropriate actuator commands, allowing higher degrees of automation and autonomy. In the end, several tasks that UAMs in current research aim to complete are given. Force application as a task was focused on and the research gaps in execution of this task by UAM were identified.

4

Aerial platforms

The aerial platform carries the manipulator to the location where it is needed, and therefore it is an integral part of the aerial manipulator. This chapter elaborates on the configuration and properties of the aerial platform. The aerial platform (actually the entire UAM) is a UAV, and section 4.1 discusses UAVs at a high level. The focus is put on multirotor vehicles because of their pervasiveness as platform for UAMs. Section 4.2 presents a taxonomy of this class of vehicles. Afterwards, section 4.3 zooms in further on the quadcopter, its properties and motivation of choosing it as the aerial platform for this research project. A brief summary of the chapter is finally presented in section 4.4.

4.1. Unmanned aerial vehicles

The study of UAVs is well-established [34] and many types of UAVs are currently in existence for different purposes. An unmanned aerial vehicle is any aeronautical vehicle that is not piloted by an on-board human. This ranges from very small, bio-inspired UAVs such as the DelFly (shown in figure 4.1) [35] to large ones such as NASA's Global Hawk (shown in figure 4.2) [36]. Most UAVs employ low levels of automatic control, such as attitude, heading, speed and altitude keeping, and are currently remotely piloted. Higher levels of control and autonomy such as path planning [37] and obstacle avoidance [38] are currently very active research areas. The long-term trend is to move to aerial systems requiring little to no human intervention.

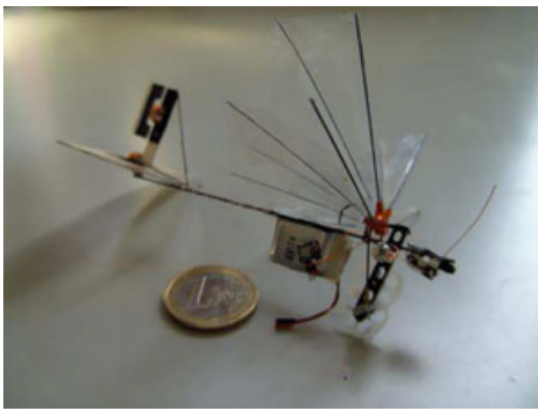

Figure 4.1: Picture of the DelFly next to a 1-euro coin as a size reference (taken from [39])

Figure 4.2: Picture of NASA's Global Hawk, with a persons standing behind it for size reference[1]

The use cases have exploded recently, and UAVs have found industrial applications in search & rescue [40], forest fire surveillance [41], oil & gas pipe monitoring [42], infrastructure inspection [43] and map-

[1] From https://www.nasa.gov/centers/armstrong/photo_feature/global_hawk_deploys_to_study_matthew.html, retrieved 19-11-2021

ping [44]. Apart from industrial and research purposes, the conventional quadcopter UAV has enjoyed great commercial success as an accessible platform for aerial photography [45], attracting both public praise and criticism.

Apart from the study of individual UAVs, studying the properties and possibilities of UAV swarms is also an active research area [46], but because of the focus on integrated aerial manipulation systems this is left out of scope.

4.2. Multirotor platforms

Multirotor UAVs are robotic vehicles that derive their aerial abilities from multiple rotary wings, giving them the ability to hover, fly slowly, demonstrate translational motion in multiple directions and vertical take-off and landing (VTOL), eliminating the need for runways and allowing take-off and landing in dense environments. These properties (VTOL in particular) make them ideal candidates for aerial manipulation systems, and multirotors are used almost exclusively in aerial manipulation applications.

As described by Hamandi *et al.* [47], five classes of aerial vehicles can be distinguished based on their actuation properties. This way of classifying is useful because it is a strong indicator of the reaction wrench an aerial manipulator can generate. While Hamandi *et al.* substantiate the actuation properties mathematically, for conciseness' sake they are described qualitatively below. The basic assumptions are that the attitude dynamics are fully actuated and non-zero force and zero moment are a feasible wrench.

Unidirectional thrust
Unidirectional thrust (UDT) refers to vehicles where the thrust vectors from the rotors are parallel in the same direction. The quadrotor is an UDT vehicle, but other UDT vehicles such as hexarotors and octorotors are also possible. UDT vehicles are the most commonplace for aerial manipulation, mainly due to the price, simplicity and ubiquity of UDT platforms. An example of a UDT platform is given in [48], where a so-called octoquad (four arms with each two propellors) UDT vehicle is used for contact inspection on the topside of the platform. This is also shown in figure 4.3(a).

Multidirectional thrust
Multidirectional thrust (MDT) vehicles can vary their thrust along more than one direction, independent from varying the moment. Strictly MDT is not used often in aerial manipulation, as in the case of more complex aerial platforms they are usually at least fully actuated. An example of a MDT platform that is not fully actuated is given by Papachristos, Alexis and Tzes [49], where a trirotor with tiltable propellors for pushing a load is presented. Although all six wrench directions can be influenced, they cannot be controlled independently, making this vehicle MDT but not FA. A visual of this platform is shown in figure 4.3(b).

Fully Actuated
Fully actuated (FA) vehicles can vary their thrust along all axes, independent from the moment. All FA vehicles are MDT, but not the other way around. Thus, FA represents a subset of MDT. FA vehicles are much more commonplace than MDT vehicles because the property of controlling all wrench components independently simplifies aerial physical interaction. This was demonstrated by Rashad, Engelen and Stramigioli [50] and Nava *et al.* [51]. A tilted propellor hexarotor is a popular configuration for fully actuated vehicles. The tilted propellor FA configuration as employed by Nava *et al.* is shown in figure 4.3(c).

Over-actuated
Over-actuated (OA) vehicles can also vary their thrust and moment along all axes independently, but with OA vehicles more than one input combination is possible. Hence, OA is a subset of FA. An OA platform was used in [52] to provide support to an ultrasonic contact inspection of oil & gas industry pipelines. In the drawing of figure 4.3(d) this rotor configuration is shown clearly. The angle β is fixed at 1/6 rad for all motors. OA platforms are not found as abundantly as OD vehicles because with the complexity this type of platform requires, OD vehicles provide more flexibility.

(a) UDT: Jimenez-Cano *et al.* [48]

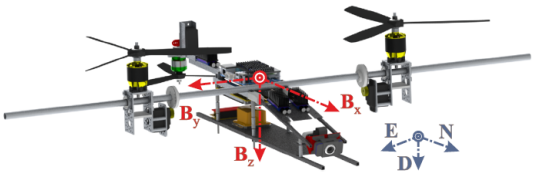

(b) MDT: Tri-TiltRotor [49]

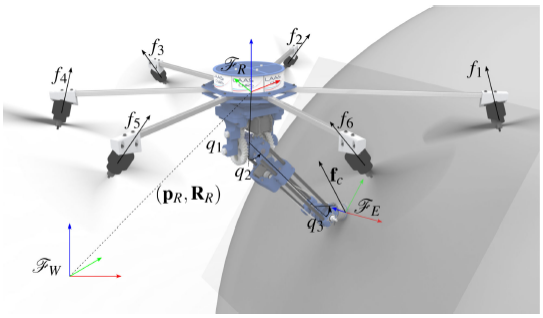

(c) FA: Nava *et al.* [51]

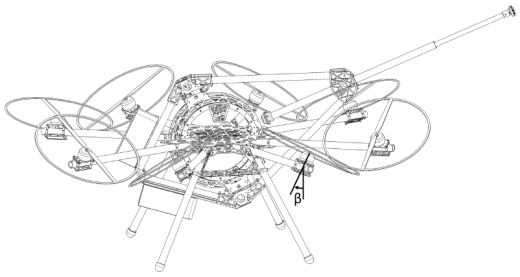

(d) OA: AeroX [52]

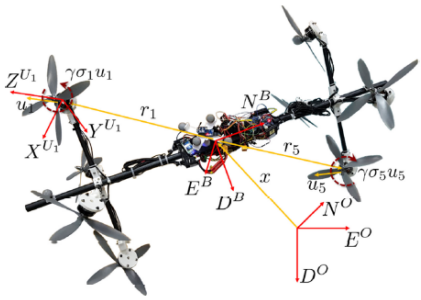

(e) OD: ODAR [16]

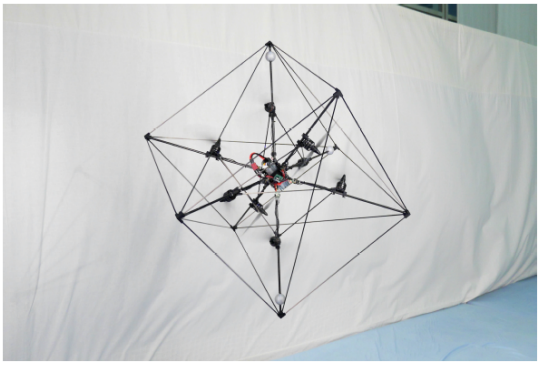

(f) OD: Omnicopter [53]

Figure 4.3: Examples of the different classes of multirotor vehicles as described by Hamandi *et al.* [47]

Omnidirectional

An omnidirectional (OD) vehicle can have its thrust assume any value in a spherical shell independent of the total moment. As such, it is also a subset of FA vehicles. OD vehicles can also be OA, but do not strictly have to be and vice versa. The difference is that an OD vehicle must be able to exert the same maximum thrust over all axes, while an OA vehicle may be able to exert a smaller thrust laterally than upwards, for example. Additionally, OA vehicles must have more than one input combination to achieve a certain wrench, while this is not necessary for OD vehicles.

An experimental example of an omnidirectional platform is ODAR [16]. This platform is able to control pose and wrench in a hybrid fashion and perform high force application. Similarly, the Omnicopter by Brescianini and D'Andrea [53] is a cube-shaped platform that is able to generate forces and moments independently and fully control its pose. Both works use eight propellors arranged in varying planes that can generate thrust in both directions to achieve omnidirectionality. Both works are shown in figure 4.3(e) and (f).

4.3. Quadrotors

In this section the focus is on UDT rotorcraft, specifically the quadrotor. The focus on this particular type of rotorcraft is due to the properties mentioned in section 4.3.1. Extra attention is given to underactuation in section 4.3.2 and finally the motivation for choosing this platform along with the assumptions made related to the coming work are given in section 4.3.3.

4.3.1. Properties

This type of rotorcraft is interesting to focus on for a couple of reasons. First, the quadrotor is capable of vertical take-off and landing (VTOL) and hover. These are extremely important properties for aerial manipulation because the bulk of aerial operations is carried out in a quasi-stationary position. Additionally, the quadrotor platform is easy to construct, contributing to its popularity. The simplicity of this multirotor design requires less expensive and heavy parts such as ESCs and DC motors. This decreases weight and cost, and improves endurance. Extensive use has also demonstrated the reliability of these platforms.

Furthermore, they have gained widespread popularity in the research community and public alike. As such, a large amount of research is readily available for these types of aerial platforms. It would be beneficial if this research can be used for and extended by aerial manipulation work.

While the quadrotor is beneficial to include based on the reasons named above, there are also reasons why the quadrotor is less suitable. The first is that quadrotors are unstable and require active control to stay in the air, but this is true for almost all multirotor vehicles. A more specific disadvantage of quadrotors is underactuation (discussed below) which results in coupled dynamics and the lack of redundancy in motors [54]. Loss of one motor means loss of control of (at least) one DoF. In industrial settings, this increases the risk of damage to assets, which is why in many industrial applications hexarotors or octorotors are used. These suffer from underactuation as well when their rotors are placed in a single plane, and as such research on underactuated vehicles is still applicable.

4.3.2. Underactuation

The underactuation property of quadrotors deserves additional discussion because it is the most influential property in the aerial manipulation context. Underactuation refers to the property that systems have less actuators than DoFs. Because of this, the pose-space cannot be arbitrarily navigated, as the dynamics of the quadrotor are coupled. This means that it is not possible for an underactuated vehicle to take any value of the pose vector statically mentioned in section 3.1.2, but rather this is constrained by the system's dynamics.

For quadrotors, the actuators are the four motors. Increasing thrust on one motor does not have an intuitive effect on the platform, so the differential flatness property [55] is exploited to allow the platform to be controlled using the more intuitive pitch, roll, yaw, and thrust commands. These are then mapped by a motor mixing algorithm to motor inputs. This qualitative explanation of the exploitation of the differential flatness property is substantiated mathematically and derived in [34].

Given the fact that the three-dimensional position and heading angle are the flat outputs, the remaining pose components (roll and pitch angle) are then distinctly not flat. The roll angle is coupled to the movement in the Y_b-direction and the pitch angle similarly to movement in the X_b-direction.

4.3.3. Motivation

Based on the properties analysed in section 4.3.1, the choice for a quadrotor as aerial platform is motivated. No platform is ever perfect, as the properties of one platform may be more suitable to a specific situation or task than another. The intended use of the platform determines the weighing of each property, and by extension the choice. In this thesis project, it is not attempted to find the optimal platform for carrying out the task at hand (accurate, substantial force application on variously oriented surfaces), but rather the goal is to find the optimal platform for adding research value.

Given the ubiquity of quadrotors, along with the simplicity in control this design brings, it is determined that this configuration is the most suitable for the purposes of this research. The simplicity of quadrotors allows for inherent advantages that cannot be found in other platforms, such as the need

for a low number of motors, ESCs, arms and accompanying flight electronics. This reduces cost and weight and increases endurance, which is favourable for adoption in both industrial/commercial as private use. Additionally, research on underactuation of quadrotors translates well to underacted hexa- and octorotors. Finally, the availability of knowledge and information on flight of quadrotors ranging from extremely applied to extremely theoretical, allowing less time to be spent on the platform and more on the UAM as a whole, is an important reason for picking this platform.

4.3.4. Assumptions

A number of assumptions regarding the aerial platform are given. These assumptions become relevant later on, with the selection of control strategy and sensor suite, as they provide a baseline for control and sensing capabilities of UAVs. The main assumptions used in later chapters are listed below.

- **On-board sensors**: the aerial platform has an on-board sensor suite consisting of a standard set of sensors such as a 9-channel IMU (3 channel accelerometer, 3 channel magnetometer and 3 axis gyroscope), barometer, GPS and downward-facing camera.
- **State availability**: the aerial platform has on-board state estimation and can estimate its own orientation with good accuracy and can estimate its own position with reasonable accuracy for navigational purposes.
- **Thrust**: it is assumed that the quadrotor can generate sufficient thrust to fly, carry a small payload and have significant thrust margin left for upwards acceleration or force exertion.

4.4. Summary

This chapter discussed the aerial platform as a vehicle for the manipulation system. The first section provided a top-level overview of the study of UAVs and has given an impression of the of the breadth of this field and identified active research areas in UAVs. The second section focused on multirotor platforms due to their universality as an aerial platform for UAMs. Five categories of platforms were identified based on their actuation properties and relevant work was cited for each category. In the next section, emphasis was placed on quadrotors (a subset of UDT vehicles), properties of this platform were identified and the choice of quadrotor as platform was motivated. Finally, the most important assumptions regarding the use of quadrotors for this research were explained.

5

Manipulation systems

Research and technology regarding the manipulation system requires understanding about some fundamental concepts in robotics. The study of robotics is very broad and established [56]. In this chapter, the relevant elements of this vast body of research are discussed along with their relationship to UAMs. To start, kinematic analysis is examined in section 5.1. This touches upon the forward and inverse kinematics, the workspace analysis and singularities. Section 5.2 discusses the most important types of mechanisms used in manipulation systems, the serial and parallel architecture. Lastly, a brief explanation and overview of the concept of compliance in the context of UAMs is given by section 5.3.

5.1. Kinematics

Kinematics is the study of points, bodies or systems of these without regard to the forces and torques that cause these motions [57]. It is useful to find out the reachable space and reach (workspace) of the manipulator's end-effector. For UAMs specifically, it is important to ensure that no collision between manipulator and rotor happens, as this would most likely create an end-of-mission scenario.

5.1.1. Forward/direct kinematics

When calculating the end-effector pose from the joint angles or other servo motor inputs, it is called forward or direct kinematics. Depending on the manipulator architecture, the calculation of the forward kinematics can range from quite simple to very challenging. This calculation is often necessary for finding the actual end-effector position from the actual servo positions.

5.1.2. Inverse kinematics

The counterpart to forward kinematics are inverse kinematics. This concerns itself with the calculation of the joint angles or servo motor setpoints based on a given end-effector position. This calculation is necessary to find the servo position reference to achieve a certain end-effector pose. The calculations are displayed visually in figure 5.1.

5.1.3. Workspace

An important consideration in the study of robotics is the determination of the possible workspace that the end-effector can reach. Workspace describes the sub-space of the complete pose-space that the end-effector can adopt. It is useful to determine to gain insight into properties like maximum reach from the base, DoFs covered by the end-effector and maximum end-effector travel. Bodie, Tognon and Siegwart show how the determination of workspace can be useful and even necessary for UAMs [58]. In this work, the desired workspace is used as an input to the manipulation system design, using a genetic optimisation algorithm to find the optimal parameter set for the parameterised manipulation system design. The manipulation system is also optimised for minimum weight and reaching a retraction point for landing.

[1] From https://nl.mathworks.com/discovery/inverse-kinematics.html, retrieved 30-11-2021.

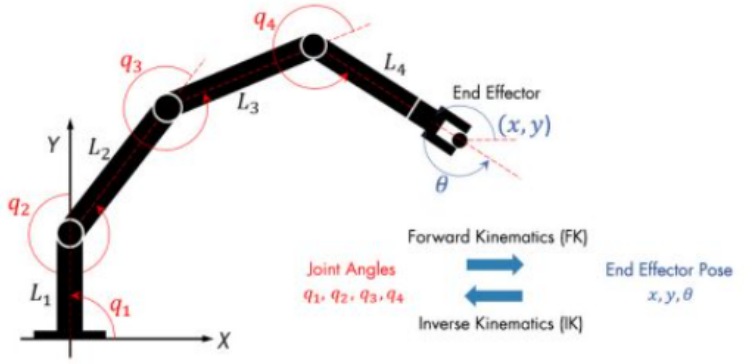

Figure 5.1: Visual represenatation of forward/direct and inverse kinematics on a serial manipulator [1]

Multiple methods for determining the workspace have been studied and proposed [59]. According to Cao *et al.*, the boundary curves (for 2D robots) and surfaces (for 3D robots) have been studied using graphical, analytical and numerical methods.

One intuitive way of determining workspace is by solving the forward kinematics of the most extreme joint angles. Given that a robot manipulator is in a singular configuration when at the workspace boundaries [60], this gives a good impression of the workspace. This approach can also be done in a Monte Carlo-style approach, sampling different actuator states to obtain a numerical estimate of the workspace.

The approach can also be applied inversely. By solving the inverse kinematics for a point in the pose-space it can be checked whether this is within reach of the manipulator.

5.1.4. Singularities

The last important subject discussed here is that of singularities. A singularity refers to a configuration in which the end-effector gets blocked in one or more directions. This means that the manipulator effectively loses one or more DoFs.

Mathematically, the joint velocities $\dot{\mathbf{q}}$ (time derivative of joint angles $\mathbf{q}$) can be calculated from the Jacobian $\mathbf{J}$ (which depends on the manipulator architecture and configuration) and the velocity vector $\mathbf{v}$ by equation (5.1).

$$\dot{\mathbf{q}} = \mathbf{J}^{-1}\mathbf{v} \tag{5.1}$$

From this equation, it is clear the inverse of the Jacobian is needed to find $\dot{\mathbf{q}}$, so when $\mathbf{J}$ is non-invertible, i.e. when its determinant is equal to 0, the manipulator is in a singularity.

Next to the actual singularity, passing through configurations close to singularities creates high joint velocities, saturating the motors so this is also not desirable.

5.2. Mechanisms

Two types of robot can be distinguished based their mechanism: serial and parallel architectures. They are explained here and their properties are elaborated upon. For a clear overview the properties are also summarised in table 5.1

Property	**Serial robot**	**Parallel robot**
Workspace	Large	Restricted
Positioning errors	Sum of joint position errors	Average of joint position errors
Mass distribution	Distributed evenly over length of kinematic chain	Concentrated at base
Rigidity	More compliant	More rigid

Table 5.1: Summary of the most relevant properties of serial and parallel robots

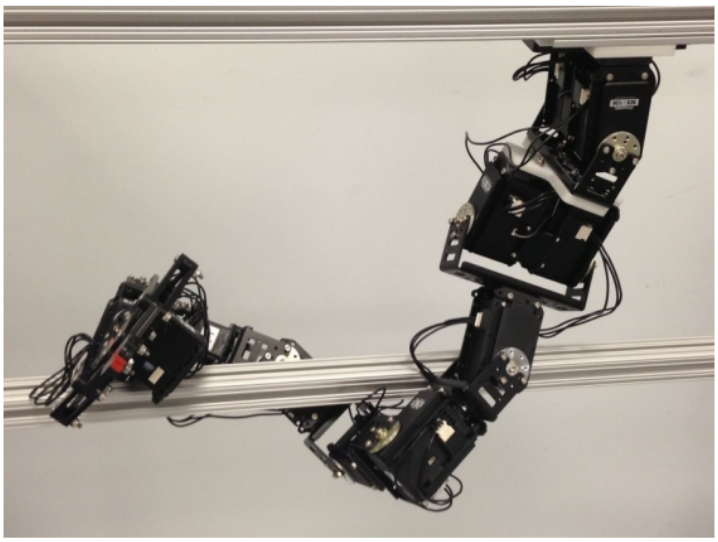

Figure 5.2: Example of how redundant DoFs in serial manipulators may be used beyond end-effector positioning [63]

5.2.1. Serial robots

The serial robot is a configuration where the joints are serially linked; the kinematic chain of the robot is open. This comes with a few properties already mentioned in table 5.1. The serial nature of this architecture allows for a much larger workspace, which is the main advantage of using serial manipulators. Especially in industrial settings, where mass (distribution) is less of a problem, disadvantages in rigidity can be counteracted by using very strong, stiff materials (such as steel).

This is not a viable option for aerial manipulators. Due to the absence of a stable base, internal forces and torques directly affect the position and attitude of the manipulator [1]. Because of this, the effect of moving masses is pronounced, and manipulation systems with little moving mass are preferred. An emphasis on lightweight serial manipulator design was shown by Suarez, Heredia and Ollero [61].

Serial manipulators also suffer from the property that the positioning errors at the end-effector are the sum of the positioning errors of the actuators. This infers the need for heavy, precise servo motors in the manipulator's joints, contributing to the unfavourable mass distribution in aerial applications. This is particularly showing in applications where the manipulator is under external loading, and has not been conclusively solved yet [62]. In controlled environments, external motion capture may be employed to accurately determine end-effector position, but in many aerial manipulation applications using the forward kinematics of the manipulator's servo positions provide a more compact, lightweight solution to determine the end-effector's position.

There are a number of works that have proposed the use of serial manipulators, and their considerable advantage in workspace and reach is not to be ignored. Danko and Oh demonstrate the use of a hyper-redundant 9 DoF serial manipulator, showing that the redundanct DoFs can be used to expand manipulation system's capabilities beyond end-effector positioning. This application is shown in figure 5.2 [63].

5.2.2. Parallel robots

The counterpart to serial robots are parallel robots. In this configuration, the kinematic chain is closed which benefits the positioning accuracy at the end-effector. Additionally, the closed kinematic chain allows the motors of the parallel robot to be placed at the base, which benefits the mass distribution for aerial applications. By placing the maniplation system's base close to the vehicle CoM, the effect of moving masses is minimised and control approaches are simplified.

Compared to serial manipulators, parallel manipulators incur penalties when it comes to workspace. The parallel architecture constrains end-effector movement which results in smaller workspaces. Another disadvantage of parallel robots is that it is not straightforward to create an arbitrary set of DoFs for the manipulation system. The DoFs are usually dependent on all actuators, meaning dynamics are highly coupled. Serial manipulators do not suffer as heavily from this, as they can have dedicated

actuators controlling each desired DoF. Because of this, a few configurations of parallel manipulator exist which are well-known and have been studied closely. These are the five-bar linkage, delta robot [64] and Gough-Stewart platform [65, 66].

Five-bar linkage
A simple parallel robot architecture is the five bar linkage. This is a planar architecture that allows the end-effector to move in the plane of the links, allowing control of the two-dimensional position. As the name suggests, it consists of a closed kinematic chain of five links and five joints, with one link being fixed to the environment (grounded) and the two adjacent joints being actuated by servo motors. The five-bar linkage has seen some popularity in aerial manipulation. Hamaza and Kovac presented an industrial quadcopter with omnidirectional workspace based around a five-bar linkage mounted on a 360° swivel, citing the limitations of serial robots mentioned above [67].

A similar configuration is used in the context of tree cavity inspection. In these works [68, 69], the five bar linkage is mounted in a perpendicular plane as the one mentioned before. The mechanism is used to position a small camera on the end-effector in tree cavities for biological research. It is shown that the mechanism can compensate aerial platform disturbances with faster dynamics and is optimised to have a sizable workspace. This manipulator is shown in figure 5.3 to illustrate the mechanism of a five-bar linkage.

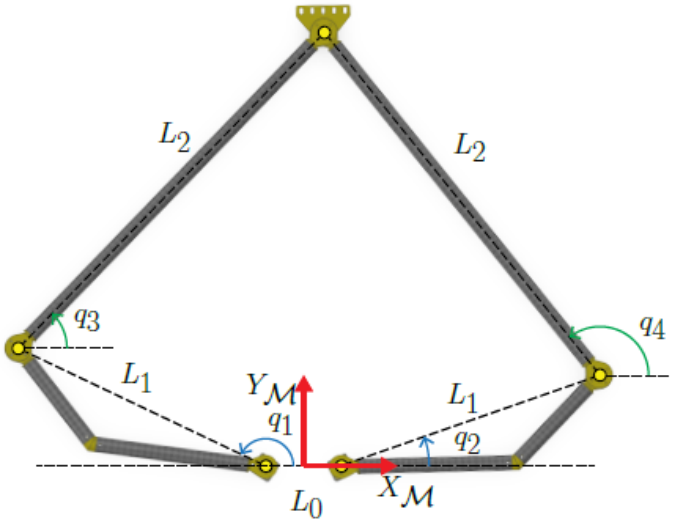

Figure 5.3: Schematic of a five-bar linkage manipulator which was used on a UAM (from [68])

Delta robot
To add a positional DoF to the five-bar linkage's workspace, the delta robot [64] can be used. This robot consists of three arms that are actuated at the base, and connected to the end-effector. The use of parallelograms in the arms maintains the orientation of the end-effector and allows movement in the three-dimensional translational space. Common applications of the delta robot are industrial pick and place operations and 3D-printing.

The delta robot is also applied in aerial manipulation. For example, the robot can be used to stabilise the end-effector for precise aerial repair [70]. Similarly, substantial positioning accuracy improvements over fixed manipulators were shown by a demonstration of aerial writing by Tzoumanikas *et al.* [14]. In other work, a delta manipulator was fitted to an OD platform to show how it could track a position reference even if the platform moves around it [58]. This configuration is shown in figure 5.4 as a visual reference. In short, the delta robot is a popular choice when it comes to applications requiring higher position accuracy than the aerial platform can provide.

Gough-Stewart platform
The Gough-Stewart platform [65, 66] is the most complex but also fully actuated 6 DoF parallel robot.

Figure 5.4: Example of a delta robot on a UAM (from [58])

It consists of a base and and end-effector (plate), which are connected by six prismatic joints allowing linear movement. The prismatic joints are actuated and connected to both the base and end-effector through universal joints. Through actuation of the six joints, full pose control is achieved, however the range of movement is limited. A 3D rendered example is shown in figure 5.5. The Gough-Stewart platform is very well-known from its application in flight simulators [71]. Another application of the Gough-Stewart platform is stabilisation of surfaces mounted on boats (which are disturbed by waves) [72]. In aerial manipulation the Gough-Stewart platform was not encountered during a survey of the literature. A hypothesised reason for this is that the inclusion of six separate active joints adds weight to the manipulator, while the extra rotational DoFs are not strictly necessary while the workspace limitations become too severe.

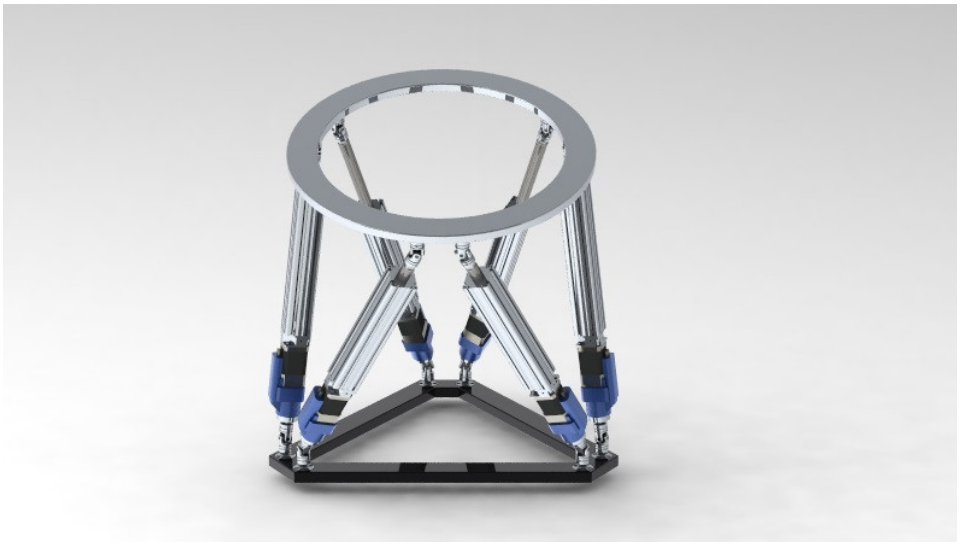

Figure 5.5: 3D render of a Gough-Stewart platform, clearly showing the six active prismatic joints[2]

[2]From https://grabcad.com/library/stewart-platform-6, retrieved 13-12-2021

5.3. Compliance

In the context of robotics, compliance refers to the concept that a robot should behave elastically when interacting with an unknown environment. This is mainly applied in the field of Human-Robot Interactin (HRI) to guarantee safety of humans occupying the same workspace as the robot [73]. The elastic behaviour makes sure that the robot does not employ full force when following a planned position trajectory, for example, but builds up resistance force as the position errors grows larger, such as in impedance control (discussed further in chapter 6). The advantage of this is that the force that is applied to the environment (or human) is not instantaneously at the maximum possible force. The implications of this for human safety are obvious; the human can move out of the way unharmed or may even be able to physically block the robot if it is compliant enough.

Compliant behaviour can generally be achieved in two ways. The use of mechanically elastic materials is the first way. This was demonstrated in the context of aerial manipulation with a manipulation system mimicking a human arm [61]. In this work, the compliance in the arm was added by introducing mechanical tendons (springs) connecting the mechanical muscles (linear actuators). In addition to providing compliance, the spring elongation could be used to estimate the payload carried by the manipulator, which is a very useful feature to incorporate in UAM modeling and control to deal with varying dynamics when carrying different payloads. The other work making use of mechanical compliance to deal with propagation of disturbances (particularly large impact disturbance) from the manipulator to the aerial platform, was done by Bartelds *et al.* [27]. In this work, a self-locking linear manipulator absorbs the shock of impact into a vertical wall by storing the impact energy in elastic bands, making it mechanically compliant. Due to this mechanism, the platform remains stable even when impacting at high velocity.

Compliance can also be achieved by using active, software-based compliance. In this type of compliance, a DoF is driven by a motor, but this motor is programmed to act as a mechanical impedance. It senses the position of the end-effector and delivers a counterforce relative to the position deviation from the nominal position. The advantage of such systems is that the stiffness (that is, the relation between position deviation and generated counterforce) is programmable: it can be varied online to accommodate different scenarios. Hamaza, Georgilas and Richardson show that this strategy in the context of aerial manipulation can be used to control the force at the end-effector and minimise the disturbances propagated to the platform due to the physical interaction [28, 74].

5.4. Summary

In this chapter, the most important concepts of robotics in the context of aerial manipulation were discussed. An overview of the fundamental kinematic concepts was given in section 5.1. From this section, it is important to do a careful workspace analysis to mitigate the risk of collision between the UAMs rotor and manipulator when their workspaces intersect. Next, parallel and serial robots are investigated and the most used parallel robot mechanisms were presented in section 5.2. It seems that for applications that do not specifically require a very large workspace w.r.t. the aerial platform, parallel manipulators seem to be the most suited because of their mass distribution and positioning accuracy. Finally, the concept of compliance was introduced and its importance is stressed in section 5.3, especially in the context of aerial manipulation. Compliance is important to facilitate the damping of disturbances that can propagate from the manipulation system to the platform and vice versa.

6

Modelling and control

In this chapter, modelling and control approaches will be discussed. Modelling and control are usually heavily intertwined since the control strategy devised for a UAM depends heavily on the design and therefore the model of the system. Typical modelling approaches are discussed in section 6.1. Next, section 6.2 dives deeper into standard control approaches in UAVs and UAMs. Sensors, discussed in section 6.3, provide the feedback data to close the loop and as such they comprise a vital part of the control system. The sensor data is then fused in a process called state estimation, briefly presented in section 6.4. Some more advanced control strategies often seen in UAMs are shown in section 6.5. Finally, section 6.6 presents the conclusions of this chapter.

6.1. System modelling

Before defining a control system, it is important to create a model of the system to be controlled. This model must define the control inputs and their effects as well as external (disturbance) influences, and must accurately reflect the kinematic behaviour of the system under these control- and external inputs. The model is then expressed in equations of motion. Two main approaches for this modelling exist: the Newtonian approach, which considers mainly the forces and torques acting on the bodies of the system and the Lagrangian approach, which considers the system's potential and kinetic energy in the study of its motion. Hamiltonian methods (similar to Lagrangian methods, but based on momentum instead of energy) are also used, but are not as popular as the other two.

According to Meng and He [12], the decoupled control approach discussed in section 3.2.3 is more suited to be modelled using the Newton-Euler equations. When using a coupled control system, however, the Langrangian method of modelling using the Euler-Lagrange formulation is preferred. A UAM model based on this approach was presented in [75].

6.2. Control

In this section, the most common control approaches in quadcopters and UAMs based on these platforms will be discussed. At first, the fast-dynamics attitude control is described in section 6.2.1. Usually, this is combined in a hierarchical fashion with the slower-dynamics position control, detailed in section 6.2.2. Lastly, because of its relevance for this work, several strategies for interaction control will be dicussed in section 6.2.3

6.2.1. Attitude control

Attitude control of quadrotors is well-known and very effective. The attitude dynamics of the UAV are fully actuated and very fast, which is exploited by the conventional controller's hierarchy [76, 77]. In basic terms, the attitude is controlled by receiving the estimated attitude from a state estimator that fuses the on-board sensor data and using this as feedback in a control loop. Usually, the Euler angles between F_b and F_E are determined. For hovering, the setpoints for pitch and roll will be zero, while the heading can take any value. For the purpose of this work, it is assumed that quadrotors can

accurately and quickly track any angular position or velocity reference that does not exceed motor saturation. When using a coupled control system, the attitude control should incorporate the dynamics of the manipulation system to account for internal moments arising from the manipulator's movements. IN decoupled control, the attitude is still influenced as the manipulator generates disturbances, but the influence is external to the control loop.

6.2.2. Position control

Position control of (quadrotor) UAVs has proven to be considerably harder than attitude control, mainly due to the difficulty in accurately estimating position without external motion capture systems such as Vicon [78] and OptiTrack [79].

The position control is often implemented as an outer loop to the (faster) attitude control loop. This way, the position error in the $X_E Y_E$-plane provides a reference for the pitch- and roll angles.
The position in the $X_E Y_E$-plane is quite vulnerable to drift when no external position determination is employed. After a dynamic movement such as flying forward, when the vehicle returns to hover some residual momentum is left (i.e. not dissipated by thrust and attitude action). This residual momentum is very hard to detect, as the accelerations due to air friction are too small for the accelerometer to register. External motion capture is extremely effective at counteracting this effect, especially indoors where accuracy is sub-centimeter. For outdoor applications, GPS can be employed with a certain degree of success, however it should be noted that this is not always available. Particularly for robots operating in industrial, cluttered environments where signals may be obstructed or reflected GPS accuracy may be rendered useless.

6.2.3. Force/interaction control

Interaction control is concerned with controlling the force and motion involved when a robotic manipulation system interacts with its environment. Pure motion planning is often not sufficiently accurate to perform delicate interaction tasks because models of the manipulation system and environment lack the required accuracy [56]. To control the interaction, compliant materials have been used in the joints and end-effectors to achieve passive compliance. For active compliance, a certain type of feedback is necessary. Two influential approaches are discussed here: impedance control and hybrid position/-force control.

Impedance control

The most widely used strategy for controlling the physical interaction in UAMs is impedance control. The concept was introduced by Prof. N. Hogan around 1984 [80, 81], as a way to control interaction between robotic manipulation systems and their environment. The philosophy here is that just controlling force or motion is not sufficient, but that there needs to be control of the dynamic behaviour of the manipulation system during interaction with the environment. This is done by controlling the relationship between exerted force and velocity. This will cause the robot to act as a mass-spring-damper system. The relation between impedance, force and velocity in the Laplace domain is shown in equation (6.1).

$$F(s) = \mathcal{L}\{M \cdot a + C \cdot v + K \cdot x\} = (Ms + C + Ks^{-1}) \cdot v = Z \cdot v \tag{6.1}$$

This has been a very successful and suitable approach to many manipulation problems, and a large number of works have shown that impedance control can be employed to manage the interaction between UAM and environment. Usually when this approach is employed, the position and force are concerned. To generate a certain force on the environment (a vertical wall), a target location inside the wall is chosen. Due to the impedance control of the system, the UAM will generate a force proportional to the distance error, i.e. if a target position deep inside the wall is chosen, the force is higher than when the target position is close to the wall's surface. This type of indirect force control typically is quite good at managing disturbances and keeping stability, but accurate control of force and position is not guaranteed.

Cataldi *et al.* [82] has shown the implementation of a multilayered coupled impedance controller, which is demonstrated on a quadcopter-based UAM with 6 DoF manipulation system. With the exception of the inverse kinematics (which depend on the manipulation system design), this approach can be translated to other UAM designs.

In the work of Ryll *et al.* [83], impedance behaviour is achieved through the use of an admittance-based controller (admittance control being the dual of impedance control). The UAM is programmed to act as a mechanical admittance and can therefore provide reaction forces to disturbances, as shown in the experiments.

Hybrid position/force control
With impedance control being an indirect force control strategy, hybrid position/force control provides a more direct way of controlling the exchanged interaction force [84]. In this method, the force and position are directly controlled, allowing stricter following of reference trajectories. This is usually applied by two complementary feedback loops, one for the motion and one for the force [2]. Although this strategy is less popular in UAMs, there are a number of works demonstrating the efficacy of hybrid position/force control. To get a force feedback signal either direct force feedback should be used, or a wrench estimator can be employed [33].

In the work of Nguyen and Lee [85], a hybrid position/force controller was presented for tools mounted rigidly on a quadrotor. By analysis of the internal dynamics, it was discovered that a condition for internal stability is that the tool-tip is that the tip on which the force acts is located above the vehicle CoG. A similarity of this situation to the simple pendulum is indicated, whereas the case where the tool-tip is under the vehicle CoG is analogous to the inverted pendulum (indicating instability).

A drawback of hybrid position/force control is that while accurate tracking of references can be achieved, it is important to define constraints. Where impedance control implicitly limits the force and displacement, this is not the case in hybrid position/force control. When the manipulator expects a force over one axis but does not encounter this, this creates a problem as displacement can escalate trying to follow the reference force.

6.3. Sensors

Sensors are essential to the functioning of a control system. They are the physical devices that facilitate the feedback data by observing the system and translating this to digital data that can be used by control software to generate a command. There are many types of sensors that can measure a great variety of physical quantities, but in this section only the sensors applicable to aerial manipulation are discussed.

6.3.1. Pose estimation

Estimation of the vehicle's own pose is often the most basic and necessary function the sensor suite needs to fulfil. To achieve this, most quadrotors (but also other UAVs) use a combination of sensors:

- Accelerometer
- Gyroscope
- Magnetometer
- (Barometric) altimeter

The combination of the first three is called an inertial measurement unit (IMU). The introduction of micro electromechanical systems (MEMS) has made strong miniturisation of these sensors possible, reducing price, weight and size drastically. For reference, an IMU module breakout board is shown in figure 6.1. The cost of this IMU is about $40.

The accelerometer measures linear accelerations over all axes. It is important to realise that this also includes the gravitational acceleration that the IMU experiences virtually at all times. Because of this property, the accelerometer has relatively low drift, but they tend to be quite noisy. Their high noise but low drift makes them useful to monitor slower dynamics, as obtaining a position estimate from a double-integrated noisy acceleration signal is unworkable. Additionally, the presence of accelerations due to motion makes solidifies the case for using the accelerometer for slow dynamics.

The gyroscope measures the angular rate of the vehicle, important for pose estimation. Gyros are generally not as noisy as accelerometers, but tend to drift heavily. By integrating the signal, it is possible to obtain the actual orientation of the vehicle, although integrating progressively worsens the errors the longer the timeframe. Because of this, they are more useful for fast dynamics over short timespans.

The accelerometer is used to keep the orientation 'grounded' by providing a reference to what the true down (gravity vector) is.

The magnetometer measures the three vector components of the magnetic field. This allows the user to obtain a heading estimate from the magnetometer. Determination of the gravity vector by the accelerometer gives a referende for pitch and roll, but not for yaw (heading), as this is a rotation about the gravity vector. By providing this measurement, the magnetometer complements the other sensors. Usually, the magnetometer works in the principle of the Hall effect.

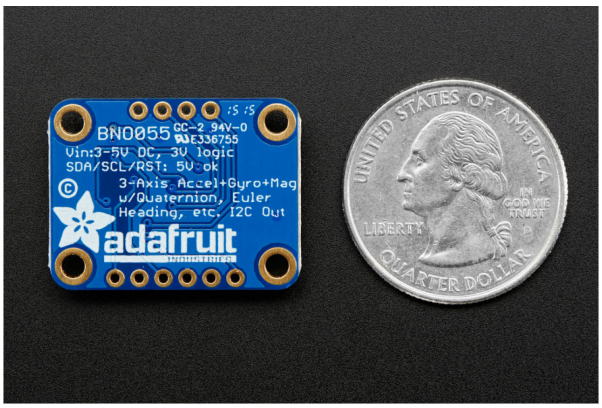

Figure 6.1: Picture of an IMU breakout board next to a quarter dollar coin, this IMU is quite large as it is on a breakout board[1].

The last sensor used in pose estimation is the altimeter. This is usually not part of a standard IMU, but it is commonly used in aerial robotics. Most altimeters work on the principle of pressure (and as such can also be referred to as barometers). The altimeter's main purpose is to strengthen the altitude estimation by measuring the pressure at ground level (at startup) and using the ground level reference with current measurements to find the altitude according to the standard atmosphere model. Taking the reference at ground level close to the of flight is necessary because larger atmospheric effects such as weather cause ambient air pressure to change spatially and temporally.

6.3.2. Remote environment perception

In more advanced aerial robotics applications, it is desirable to employ remote sensing techniques to obtain data on the environment of the vehicle, rather than only the vehicle itself. To this end, a number of remote sensing technologies have gained popularity lately. The most important ones that will be discussed here are the rangefinder, LiDAR (type of rangefinder) and visual camera.

Data extraction and subsequent control based on visual imaging is an entire research field on its own, and is very active at this moment. This has been driven by the increase of available processing power on virtually all platforms, coupled with the decrease in price, mass and size of camera modules. Visual servoing in aerial manipulation was shown in [86].

LiDAR is a technology similar to radar, but using laser light. A laser beam is expelled from the sensor, which waits until it detects the specific wavelength returning. By measuring the time of flight (ToF), the distance to the reflecting object can be determined. This principle only allows LiDAR to 'see' objects in a direct line of sight. LiDAR modules are typically quite heavy and bulky, but smaller modules are emerging and use in unmanned flight is growing. An advantage of LiDAR is the spatial and temporal resolution of the data, as well as the accuracy, which are all very good. It was used in infrastructure inspection by drone by Ikeda *et al.* [5, 32], but this platform had to be very large to be able to support a LiDAR system because of the weight and power consumption.

Other rangefinding techniques are also employed. Common examples include a sonic rangefinder, which can also be used as an altimeter by pointing it downwards. Sonic rangefinders use acoustic waves and their reflection for distance estimations.

[1] From https://www.kiwi-electronics.nl/nl/adafruit-9-dof-absolute-orientation-imu-fusion-breakout-bno055-1996, retrieved 13-12-2021

6.3.3. Force sensing

In principle, the two physical phenomena on which force measurement is conventionally based are piezoelectric materials and mechanical strain. Piezoelectric materials (such as quartz) produce an electrical potential under mechanical stress. This potential is linear with the amount of stress experienced, and can be amplified and measured as an input signal to a processor or controller. Piezoelectric force sensors are applicable on very small to very large forces and the displacement is much smaller than with typical load cells and strain gauges. A large disadvantage of piezoelectric sensors is that the charge that is indicative of the force is lost over time, so long-term measurements display a heavy drift.

Force measurement based on mechanical strain is widespread and mainly uses strain gauges as transducer. Strain gauges consist of elastic, nonconductive material with a conductor 'printed' on it in folded arrangements. Due to the arrangement of the conductor, a current across the gauge experiences a certain resistance. When strain is applied the gauge deforms, and because of this deformation the resistance changes, which can then be measured. Because strain is linear with stress in the elastic region of the stress-strain curve, this resistance provides a good indication of the actual stress (and thus force if multiplied by the load cell's surface area). Strain gauges are very cost-efficient but they do display wear under cyclic loading due to fatigue of the material.

6.4. State estimation

State estimation refers to the processing of sensor data to obtain an accurate, reliable estimation of the current state of the vehicle. In this context, the state can be described by any variable, but in the context of aerial robotics, certain parameters can hardly be omitted. The three principle orientation angles are consistently a central part of the estimation, as well as altitude and possible the other location coordinates.

As with visual data processing, state estimation is an active research field in itself. Established techniques are mostly based on filtering (specifically the complementary filter and Kalman filter, along with all its variations), but new techniques such as simultaneous localisation and mapping (SLAM) are also getting attention and viability.

6.4.1. Kalman filter

The Kalman filter [87], also called linear quadratic estimator (LQE) is an algorithm that uses prior knowledge and sensor measurements to come up with an estimate of the state. These estimates are usually more accurate than actual measurements, because measurements are influenced by measurement noise. The Kalman filter employs an internal model of the system which it uses to create predictions of the state. By assuming disturbance and measurement noise to be Gaussian, a confidence in own predictions can be calculated. When confidence in the internal predictions are right, the output estimate will skew more towards the modelled prediction, and when the confidence in the prediction is low, the output estimate skews more towards the sensor input. This internal prediction also increases robustness when measurements are of varying quality (such as with GPS).

The most well-known and important extensions of the Kalman filter are the Extended Kalman filter (EKF) and Unscented Kalman filter (UKF), which extend the application domain to include nonlinear systems. Kamel, Burri and Siegwart employ an EKF for state estimation in [68].

6.4.2. SLAM

Simultaneous localisation and mapping (SLAM) is a process by which a mobile platform can map its environment and at the same time determine its location in the created map [88]. The SLAM problem is present in many disciplines related to mobile robotics, and as such it is a very active research area. In the context of aerial manipulation, SLAM may be employed to identify targets of the manipulation operation and simultaneously determine the UAMs location with respect to this target. Two problems present themselves with this approach: sensors and computational complexity. Common sensors used in SLAM are the ones mentioned in section 6.3.2 and will not be elaborated further.

Computational complexity is the other problem. While advances in computational power are still made, there have been observations that Moore's law may be approaching a limit for a number of years

[89]. Coupled with the weight- and power constraints of mobile robotics, it is clear computational power is limited and should be a consideration. Many SLAM algorithms are too computationally complex to run on the type of electronics that is commonly employed as flight computer nowadays (such as the Raspberry Pi). This problem is currently recognised by the SLAM community, and efforts are made to unite the desired performance with lower computational requirements [90].

6.5. Advanced controllers

Many aerial manipulation works use more advanced control strategies than the ones discussed so far, mainly due to the nonlinear nature of UAM's dynamics. A very popular nonlinear advanced control strategy is model predictive control (MPC). MPC is an optimal control strategy that relies on an internal model of the system. Using this internal model, the controller performs an optimisation of the input signal over a receding horizon of multiple timesteps, finding the optimal input signal to follow the reference trajectory. It then executes this input only for the first timestep, and performs the optimisation again.

Because of the need for optimisations over multiple timesteps for every control action, the computational requirements for MPC can be quite heavy. In [91], a comparison study between linear and nonlinear MPC is executed. The experimental platform contains an Intel 3.1 GHz i7 Core processor, which is quite heavy for an on-board aerial computational resource.

6.6. Summary

This chapter described important concepts related to control in the context of aerial manipulation. The chapter started with an overview of the modelling strategies (Newtonian, Lagrangian or Hamiltonian) that can be used, as the establishment of a model is integral to the design of an appropriate controller. Next, fundamental control concepts in attitude, position and interaction (force) control were discussed, as these are the most important states to control in a force application scenario. The sensors that are used as feedback devices in the control loops were discussed afterwards, and it was discovered that the availability, cost and quality of sensors have a big impact on the chosen control strategy. State estimation from sensor data was discussed after, zooming in on the Kalman filter and SLAM as important concepts in the context of aerial manipulation. Finally, a short discussion on advanced controllers was presented which observes the popularity of MPC, although it is computationally intensive.

7

Conclusion

In this chapter the conclusions from this literature review are summarised. The conclusions from the literature study are used to support the experimental methodology by providing pointers for experiment design.
It is clear that aerial manipulation is rapidly developing from a new, highly experimental and trial-and-error based research field into a discipline that makes great strides towards being fundamentally understood and clearly structured. There are promises of great industrial potential leading to increases in safety and reductions in cost, which attract investment from public parties (evidenced by public projects such as Aeroworks, SHERPA and AEROARMS) and undoubtedly private parties alike.

Many different applications of aerial manipulation have been investigated in the past decade, and even though the recent demonstrations from the scientific community look hopeful, there are still aspects that should be investigated deeper. It was identified that even though a number of works demonstrate the constituent parts of a system capable of applying a substantial controlled force to complex shapes, such an integrated system has not been described in literature yet. The hypothesis is that through the use of a parallel manipulator and an integrated coupled control system (controlling manipulator and platform simultaneously) higher forces and position accuracy of the end-effector can be achieved using a conventional quadrotor platform.

From a study on aerial platforms it was determined that while omnidirectionally fully actuated platforms exist, they cannot compare to the conventional quadrotor configuration in terms of knowledge availability and price due to the ubiquity of the latter. Because of this, research in this thesis will be carried out using a quadrotor platform. Several works exploiting the attitude of the quadrotor for higher force application were found, and this property is not investigated further despite its potential. For this research the quadrotor is used as platform because of the reasons mentioned above and to further investigate exploiting quadrotor attitude to exert higher magnitude forces on the environment.

Regarding the manipulator there are a number of examples exploiting the manipulator's fast dynamics to compensate for the slower position inaccuracies of the aerial platform. Additionally, it has been shown that including compliance (either passive or active) in the manipulator decreases the propagation of sudden disturbances from the environment to the aerial platform, increasing safety as the platform's attitude controller does not deal with sudden large disturbances. The addition of DoFs in the manipulator has advantages in both allowing active compliance and position disturbance rejection as described above. Furthermore, given the positioning accuracy and mass distribution parallel robots offer a superior performance to their serial counterparts. The workspace advantage of serial robots is less relevant for aerial manipulators, because they derive their workspace advantage from the aerial platform. To allow compensation for platform positioning accuracies and compliance, high-DoF manipulation systems are desirable. For the reasons mentioned before, in this research a parallel delta robot (3 DoF) mounted on two rotational DoFs (pitch and yaw) will be used.

From the research carried out over the last decade, it shows that coupled control systems, where the manipulator and aerial platform are controlled by the same controller, are able to achieve more accurate control. This finding supports the holistic design philosophy found in many other aerospace projects. Concerning the force feedback it was determined to be advantageous to incorporate a force

sensor in the manipulator for direct feedback. Along with providing a direct feedback signal on the applied force, this configuration also allows exploration of interaction with compliant environments as the exchanged force between end-effector and environment can be measured. A problem in the aerial manipulation space also consists of accurate position determination without the need for external motion capture systems. To keep within the scope of this research project, this problem will be left for other research. In this project, the focus will be on design and experimentation with a centralised hybrid position/force controller for the earlier proposed aerial manipulation system to achieve high force- and position accuracy tracking of the end-effector.

There is still a need to do more research into aerial manipulation for this technology to fully mature. From the research gaps that were found in this literature study, the focus of this research will be on the design of a centralised hybrid position/force controller, with which experiments will be done on the proposed aerial manipulation system. The goal is to show that an integrated approach allows for more accurate control over the applied force and the location where this force is applied.

References

[1] H.B. Khamseh, F. Janabi-Sharifi, and A. Abdessameud. “Aerial manipulation—A literature survey”. In: *Robotics and Autonomous Systems* 107 (2018), pp. 221–235.

[2] A. Ollero et al. “Past, Present, and Future of Aerial Robotic Manipulators”. In: *IEEE Transactions on Robotics* (2021).

[3] A. Albers et al. “Semi-autonomous flying robot for physical interaction with environment”. In: *2010 IEEE Conference on Robotics, Automation and Mechatronics*. IEEE. 2010, pp. 441–446.

[4] M. Orsag et al. “Valve turning using a dual-arm aerial manipulator”. In: *2014 international conference on unmanned aircraft systems (ICUAS)*. IEEE. 2014, pp. 836–841.

[5] T. Ikeda et al. “Wall contact by octo-rotor UAV with one DoF manipulator for bridge inspection”. In: *2017 IEEE/RSJ International Conference on Intelligent Robots and Systems (IROS)*. IEEE. 2017, pp. 5122–5127.

[6] H. Seo, S. Kim, and H.J. Kim. “Aerial grasping of cylindrical object using visual servoing based on stochastic model predictive control”. In: *2017 IEEE international conference on robotics and automation (ICRA)*. IEEE. 2017, pp. 6362–6368.

[7] B.B. Kocer et al. “Inspection-while-flying: An autonomous contact-based nondestructive test using uav-tools”. In: *Automation in Construction* 106 (2019), p. 102895.

[8] J.A. Mulder et al. *Flight Dynamics*. Course reader. Mar. 2013.

[9] F. Ruggiero, V. Lippiello, and A. Ollero. “Aerial manipulation: A literature review”. In: *IEEE Robotics and Automation Letters* 3.3 (2018), pp. 1957–1964.

[10] D. Xilun et al. “A review of aerial manipulation of small-scale rotorcraft unmanned robotic systems”. In: *Chinese Journal of Aeronautics* 32.1 (2019), pp. 200–214.

[11] A. Mohiuddin et al. “A survey of single and multi-UAV aerial manipulation”. In: *Unmanned Systems* 8.02 (2020), pp. 119–147.

[12] X. Meng, Y. He, and J. Han. “Survey on aerial manipulator: System, modeling, and control”. In: *Robotica* 38.7 (2020), pp. 1288–1317.

[13] M. Orsag et al. *Aerial manipulation*. Springer, 2018.

[14] D. Tzoumanikas et al. “Aerial manipulation using hybrid force and position nmpc applied to aerial writing”. In: *arXiv preprint arXiv:2006.02116* (2020).

[15] H.W. Wopereis et al. “Application of substantial and sustained force to vertical surfaces using a quadrotor”. In: *2017 IEEE international conference on robotics and automation (ICRA)*. IEEE. 2017, pp. 2704–2709.

[16] S. Park et al. “Odar: Aerial manipulation platform enabling omnidirectional wrench generation”. In: *IEEE/ASME Transactions on mechatronics* 23.4 (2018), pp. 1907–1918.

[17] K. Bodie et al. “An omnidirectional aerial manipulation platform for contact-based inspection”. In: *arXiv preprint arXiv:1905.03502* (2019).

[18] S.A. Conyers, M.J. Rutherford, and K.P. Valavanis. “An empirical evaluation of ceiling effect for small-scale rotorcraft”. In: *2018 International Conference on Unmanned Aircraft Systems (ICUAS)*. IEEE. 2018, pp. 243–249.

[19] S. Hamaza et al. “Sensor installation and retrieval operations using an unmanned aerial manipulator”. In: *IEEE Robotics and Automation Letters* 4.3 (2019), pp. 2793–2800.

[20] F. Huber et al. “First analysis and experiments in aerial manipulation using fully actuated redundant robot arm”. In: *2013 IEEE/RSJ International Conference on Intelligent Robots and Systems*. IEEE. 2013, pp. 3452–3457.

[21] M. Bernard and K. Kondak. “Generic slung load transportation system using small size helicopters”. In: *2009 IEEE International Conference on Robotics and Automation*. IEEE. 2009, pp. 3258–3264.

[22] C. Papachristos, K. Alexis, and A. Tzes. “Efficient force exertion for aerial robotic manipulation: Exploiting the thrust-vectoring authority of a tri-tiltrotor uav”. In: *2014 IEEE international conference on robotics and automation (ICRA)*. IEEE. 2014, pp. 4500–4505.

[23] P.E.I. Pounds, D.R. Bersak, and A.M. Dollar. “Grasping from the air: Hovering capture and load stability”. In: *2011 IEEE international conference on robotics and automation*. IEEE. 2011, pp. 2491–2498.

[24] F. Augugliaro et al. “The flight assembled architecture installation: Cooperative construction with flying machines”. In: *IEEE Control Systems Magazine* 34.4 (2014), pp. 46–64.

[25] G. Hunt et al. “3D printing with flying robots”. In: *2014 IEEE international conference on robotics and automation (ICRA)*. IEEE. 2014, pp. 4493–4499.

[26] J.L.J. Scholten et al. “Interaction control of an UAV endowed with a manipulator”. In: *2013 IEEE International Conference on Robotics and Automation*. IEEE. 2013, pp. 4910–4915.

[27] T. Bartelds et al. “Compliant aerial manipulators: Toward a new generation of aerial robotic workers”. In: *IEEE Robotics and Automation Letters* 1.1 (2016), pp. 477–483.

[28] S. Hamaza, I. Georgilas, and T. Richardson. “An adaptive-compliance manipulator for contact-based aerial applications”. In: *2018 IEEE/ASME International Conference on Advanced Intelligent Mechatronics (AIM)*. IEEE. 2018, pp. 730–735.

[29] X. Meng et al. “Contact force control of an aerial manipulator in pressing an emergency switch process”. In: *2018 IEEE/RSJ International Conference on Intelligent Robots and Systems (IROS)*. IEEE. 2018, pp. 2107–2113.

[30] X. Meng et al. “Force-Sensorless Contact Force Control of an Aerial Manipulator System”. In: *2018 IEEE International Conference on Real-time Computing and Robotics (RCAR)*. IEEE. 2018, pp. 595–600.

[31] D.R. McArthur, A.B. Chowdhury, and D.J. Cappelleri. “Design of the I-BoomCopter UAV for environmental interaction”. In: *2017 IEEE international conference on robotics and automation (ICRA)*. IEEE. 2017, pp. 5209–5214.

[32] T. Ikeda et al. “Stable impact and contact force control by UAV for inspection of floor slab of bridge”. In: *Advanced Robotics* 32.19 (2018), pp. 1061–1076.

[33] S. Bellens, J. De Schutter, and H. Bruyninckx. “A hybrid pose/wrench control framework for quadrotor helicopters”. In: *2012 IEEE International Conference on Robotics and Automation*. IEEE. 2012, pp. 2269–2274.

[34] K.P. Valavanis and G.J. Vachtsevanos. *Handbook of unmanned aerial vehicles*. Vol. 2077. Springer, 2015.

[35] G.C.H.E. De Croon et al. “Design, aerodynamics and autonomy of the DelFly”. In: *Bioinspiration & biomimetics* 7.2 (2012), p. 025003.

[36] J.C. Naftel. *NASA Global Hawk: a new tool for Earth science research*. National Aeronautics and Space Administration, Dryden Flight Research Center, 2009.

[37] L. Yang et al. “A literature review of UAV 3D path planning”. In: *Proceeding of the 11th World Congress on Intelligent Control and Automation*. IEEE. 2014, pp. 2376–2381.

[38] B.M. Albaker and N.A. Rahim. “A survey of collision avoidance approaches for unmanned aerial vehicles”. In: *2009 international conference for technical postgraduates (TECHPOS)*. IEEE. 2009, pp. 1–7.

[39] G.C.H.E. De Croon et al. *The delfly*. Vol. 10. Springer, 2016, pp. 978–94.

[40] S. Waharte and N. Trigoni. “Supporting search and rescue operations with UAVs”. In: *2010 International Conference on Emerging Security Technologies*. IEEE. 2010, pp. 142–147.

[41] D.W. Casbeer et al. “Cooperative forest fire surveillance using a team of small unmanned air vehicles”. In: *International Journal of Systems Science* 37.6 (2006), pp. 351–360.

[42] C. Gómez and D.R. Green. “Small unmanned airborne systems to support oil and gas pipeline monitoring and mapping”. In: *Arabian Journal of Geosciences* 10.9 (2017), p. 202.

[43] H. Shakhatreh et al. “Unmanned aerial vehicles (UAVs): A survey on civil applications and key research challenges”. In: *Ieee Access* 7 (2019), pp. 48572–48634.

[44] F. Nex and F. Remondino. “UAV for 3D mapping applications: a review”. In: *Applied geomatics* 6.1 (2014), pp. 1–15.

[45] O.B. Waxman. “Aerial Photography Has Changed the World. Drones Are Just the Latest Example”. In: *Time* (May 2018). URL: `https://time.com/5281295/aerial-photography-history-drones/`.

[46] A. Bürkle, F. Segor, and M. Kollmann. “Towards autonomous micro uav swarms”. In: *Journal of intelligent & robotic systems* 61.1 (2011), pp. 339–353.

[47] M. Hamandi et al. “Design of multirotor aerial vehicles: A taxonomy based on input allocation”. In: *The International Journal of Robotics Research* 40.8-9 (2021), pp. 1015–1044.

[48] A.E. Jimenez-Cano et al. “Aerial manipulator for structure inspection by contact from the underside”. In: *2015 IEEE/RSJ international conference on intelligent robots and systems (IROS)*. IEEE. 2015, pp. 1879–1884.

[49] C. Papachristos, K. Alexis, and A. Tzes. “Dual–authority thrust–vectoring of a tri–tiltrotor employing model predictive control”. In: *Journal of intelligent & robotic systems* 81.3-4 (2016), pp. 471–504.

[50] R. Rashad, J.B.C. Engelen, and S. Stramigioli. “Energy tank-based wrench/impedance control of a fully-actuated hexarotor: A geometric port-hamiltonian approach”. In: *2019 International Conference on Robotics and Automation (ICRA)*. IEEE. 2019, pp. 6418–6424.

[51] G. Nava et al. “Direct force feedback control and online multi-task optimization for aerial manipulators”. In: *IEEE Robotics and Automation Letters* 5.2 (2019), pp. 331–338.

[52] M.Á. Trujillo et al. “Novel aerial manipulator for accurate and robust industrial NDT contact inspection: A new tool for the oil and gas inspection industry”. In: *Sensors* 19.6 (2019), p. 1305.

[53] D. Brescianini and R. D’Andrea. “Design, modeling and control of an omni-directional aerial vehicle”. In: *2016 IEEE international conference on robotics and automation (ICRA)*. IEEE. 2016, pp. 3261–3266.

[54] B.J. Emran and H. Najjaran. “A review of quadrotor: An underactuated mechanical system”. In: *Annual Reviews in Control* 46 (2018), pp. 165–180.

[55] M. Van Nieuwstadt, M. Rathinam, and R.M. Murray. “Differential flatness and absolute equivalence”. In: *Proceedings of 1994 33rd IEEE Conference on Decision and Control*. Vol. 1. IEEE. 1994, pp. 326–332.

[56] B. Siciliano, O. Khatib, and T. Kröger. *Springer handbook of robotics*. Vol. 200. Springer, 2008.

[57] K.J. Waldron and J. Schmiedeler. “Kinematics”. In: *Springer handbook of robotics*. Springer, 2016, pp. 11–36.

[58] K. Bodie, M. Tognon, and R. Siegwart. “Dynamic End Effector Tracking with an Omnidirectional Parallel Aerial Manipulator”. In: *IEEE Robotics and Automation Letters* 6.4 (2021), pp. 8165–8172.

[59] Y. Cao et al. “Accurate numerical methods for computing 2d and 3d robot workspace”. In: *International Journal of Advanced Robotic Systems* 8.6 (2011), p. 76.

[60] F.L. Litvin. “Application of theorem of implicit function system existence for analysis and synthesis of linkages”. In: *Mechanism and Machine Theory* 15.2 (1980), pp. 115–125.

[61] A. Suarez, G. Heredia, and A. Ollero. “Lightweight compliant arm with compliant finger for aerial manipulation and inspection”. In: *2016 IEEE/RSJ International Conference on Intelligent Robots and Systems (IROS)*. IEEE. 2016, pp. 4449–4454.

[62] H.P. Jawale and H.T. Thorat. “Positional error estimation in serial link manipulator under joint clearances and backlash”. In: *Journal of Mechanisms and Robotics* 5.2 (2016), p. 021003.

[63] T.W. Danko and P.Y. Oh. “A hyper-redundant manipulator for mobile manipulating unmanned aerial vehicles”. In: *2013 international conference on unmanned aircraft systems (ICUAS)*. IEEE. 2013, pp. 974–981.

[64] F. Pierrot, C. Reynaud, and A. Fournier. “DELTA: a simple and efficient parallel robot”. In: *Robotica* 8.2 (1990), pp. 105–109.

[65] V.E. Gough. “Contribution to discussion of papers on research in automobile stability, control and tyre performance”. In: *Proc. of Auto Div. Inst. Mech. Eng.* 171 (1957), pp. 392–395.

[66] D. Stewart. “A platform with six degrees of freedom”. In: *Proceedings of the institution of mechanical engineers* 180.1 (1965), pp. 371–386.

[67] S. Hamaza and M. Kovac. “Omni-Drone: on the Design of a Novel Aerial Manipulator with Omnidirectional Workspace”. In: *2020 17th International Conference on Ubiquitous Robots (UR)*. IEEE. 2020, pp. 153–158.

[68] M. Kamel, K. Alexis, and R. Siegwart. “Design and modeling of dexterous aerial manipulator”. In: *2016 IEEE/RSJ International Conference on Intelligent Robots and Systems (IROS)*. IEEE. 2016, pp. 4870–4876.

[69] K. Steich et al. “Tree cavity inspection using aerial robots”. In: *2016 IEEE/RSJ International Conference on Intelligent Robots and Systems (IROS)*. IEEE. 2016, pp. 4856–4862.

[70] P. Chermprayong et al. “An integrated delta manipulator for aerial repair: A new aerial robotic system”. In: *IEEE Robotics & Automation Magazine* 26.1 (2019), pp. 54–66.

[71] O. Stroosma, M.M. Van Paassen, and M. Mulder. “Using the SIMONA research simulator for human-machine interaction research”. In: *AIAA modeling and simulation technologies conference and exhibit*. 2003, p. 5525.

[72] C. Salzmann and D. Julio. “Ampelmann: Development of the access system for offshore wind turbines”. PhD thesis. Delft University of Technology, 2010.

[73] M. Van Damme et al. “The role of compliance in robot safety”. In: *Proceedings of the Seventh IARP Workshop on Technical Challenges for Dependable Robots in Human Environments*. 2010, pp. 65–71.

[74] S. Hamaza, I. Georgilas, and T. Richardson. “Towards an adaptive-compliance aerial manipulator for contact-based interaction”. In: *2018 IEEE/RSJ International Conference on Intelligent Robots and Systems (IROS)*. IEEE. 2018, pp. 1–9.

[75] V. Lippiello and F. Ruggiero. “Cartesian impedance control of a UAV with a robotic arm”. In: *IFAC Proceedings Volumes* 45.22 (2012), pp. 704–709.

[76] R. Mahony and T. Hamel. “Robust trajectory tracking for a scale model autonomous helicopter”. In: *International Journal of Robust and Nonlinear Control: IFAC-Affiliated Journal* 14.12 (2004), pp. 1035–1059.

[77] K. Nonami et al. *Autonomous flying robots: unmanned aerial vehicles and micro aerial vehicles*. Springer Science & Business Media, 2010.

[78] *Vicon | Award winning Motion Capture Systems*. Nov. 2021. URL: `https://www.vicon.com/`.

[79] *OptiTrack - Motion Capture Systems*. Dec. 2021. URL: `https://optitrack.com/`.

[80] N. Hogan. “Impedance control: An approach to manipulation: Part I—Theory”. In: (1985).

[81] N. Hogan. “Impedance control: An approach to manipulation: Part II—Implementation”. In: (1985).

[82] E. Cataldi et al. “Impedance control of an aerial-manipulator: Preliminary results”. In: *2016 IEEE/RSJ International Conference on Intelligent Robots and Systems (IROS)*. IEEE. 2016, pp. 3848–3853.

[83] M. Ryll et al. “6D physical interaction with a fully actuated aerial robot”. In: *2017 IEEE International Conference on Robotics and Automation (ICRA)*. IEEE. 2017, pp. 5190–5195.

[84] M.H. Raibert and J.J. Craig. “Hybrid position/force control of manipulators”. In: (1981).

[85] H.N. Nguyen and D. Lee. “Hybrid force/motion control and internal dynamics of quadrotors for tool operation”. In: *2013 IEEE/RSJ International Conference on Intelligent Robots and Systems*. IEEE. 2013, pp. 3458–3464.

[86] A. Santamaria-Navarro et al. “Uncalibrated visual servo for unmanned aerial manipulation”. In: *IEEE/ASME Transactions on Mechatronics* 22.4 (2017), pp. 1610–1621.

[87] G. Welch, G. Bishop, et al. “An introduction to the Kalman filter”. In: (1995).

[88] T. Bailey and H. Durrant-Whyte. “Simultaneous localization and mapping (SLAM): Part II”. In: *IEEE robotics & automation magazine* 13.3 (2006), pp. 108–117.

[89] M. Lundstrom. “Moore’s law forever?” In: *Science* 299.5604 (2003), pp. 210–211.

[90] M. Abouzahir et al. “Embedding SLAM algorithms: Has it come of age?” In: *Robotics and Autonomous Systems* 100 (2018), pp. 14–26.

[91] M. Kamel, M. Burri, and R. Siegwart. “Linear vs nonlinear MPC for trajectory tracking applied to rotary wing micro aerial vehicles”. In: *IFAC-PapersOnLine* 50.1 (2017), pp. 3463–3469.

Part III

Appendices

A

Kinematic Model

A.1 Homogeneous Transformation Matrices

These are the single homogeneous transformation matrices following from the Denavit-Hartenberg parameters presented in Table 1. Multiplying these will yield the kinematics of the end-effector in $\mathcal{F}_I$.

$$H_b^I = \begin{bmatrix} c\theta c\psi & s\varphi s\theta c\psi - c\varphi s\psi & c\varphi s\theta c\psi + s\varphi s\psi & x \\ c\theta s\psi & s\varphi s\theta s\psi + c\varphi c\psi & c\varphi s\theta s\psi - s\varphi c\psi & y \\ -s\theta & s\varphi c\theta & c\varphi c\theta & z \\ 0 & 0 & 0 & 1 \end{bmatrix}$$

$$H_1^b = \begin{bmatrix} 1 & 0 & 0 & 0 \\ 0 & 0 & 1 & 0 \\ 0 & -1 & 0 & -L_1 \\ 0 & 0 & 0 & 1 \end{bmatrix}$$

$$H_2^1 = \begin{bmatrix} -sq_1 & 0 & cq_1 & -L_2 sq_1 \\ cq_1 & 0 & sq_1 & L_2 cq_1 \\ 0 & 1 & 0 & 0 \\ 0 & 0 & 0 & 1 \end{bmatrix}$$

$$H_3^2 = \begin{bmatrix} -1 & 0 & 0 & 0 \\ 0 & 0 & 1 & 0 \\ 0 & 1 & 0 & q_2 + L_3 L_4 \\ 0 & 0 & 0 & 1 \end{bmatrix}$$

$$H_{ee}^3 = \begin{bmatrix} -sq_3 & 0 & cq_3 & -L_5 sq_3 \\ cq_3 & 0 & sq_3 & L_5 cq_3 \\ 0 & 1 & 0 & 0 \\ 0 & 0 & 0 & 1 \end{bmatrix}$$

A.2 Kinematics function

Below the full forward kinematics function is documented.

$$\boldsymbol{k}(\boldsymbol{\xi}) = \begin{bmatrix} x_{ee} & y_{ee} & z_{ee} & \psi_{ee} & \theta_{ee} & \varphi_{ee} \end{bmatrix}^\top$$

$$\begin{aligned}
x_{ee} =& x - (s\varphi s\psi + c\varphi c\psi s\theta)(L_1 + sq_1(L_4 + q_2) + \\
& L_5 s(q_1 + q_3) + L_2 cq_1 + L_3 sq_1) + c\psi c\theta(cq_1(L_4 + q_2) + \\
& L_5 c(q_1 + q_3) + L_3 cq_1 - L_2 sq_1) \\
y_{ee} =& y + (c\psi s\varphi - c\varphi s\psi s\theta)(L_1 + sq_1(L_4 + q_2) + \\
& L_5 s(q_1 + q_3) + L_2 cq_1 + L_3 sq_1) + c\theta s\psi(cq_1(L_4 + q_2) + \\
& L_5 c(q_1 + q_3) + L_3 cq_1 - L_2 sq_1) \\
z_{ee} =& z - s\theta(cq_1(L_4 + q_2) + L_5 c(q_1 + q_3) + L_3 cq_1 - L_2 sq_1) - \\
& c\varphi c\theta(L_1 + sq_1(L_4 + q_2) + L_5 s(q_1 + q_3) + L_2 cq_1 + L_3 sq_1) \\
\psi_{ee} =& -\arctan((s(q_1 + q_3)(c\psi s\varphi - c\varphi s\psi s\theta) + c(q_1 + q_3)c\theta s\psi)/ \\
& (s(q_1 + q_3)(s\varphi s\psi + c\varphi c\psi s\theta) - c(q_1 + q_3)c\psi c\theta)) \\
\theta_{ee} =& \arcsin(c(q_1 + q_3)s\theta + s(q_1 + q_3)c\varphi c\theta) \\
\varphi_{ee} =& -\arctan((c\theta s\varphi)/(s(q_1 + q_3)s\theta - c(q_1 + q_3)c\varphi c\theta))
\end{aligned}$$

A.3 Full Jacobian

$$J = \begin{bmatrix} 1 & 0 & 0 & J_{1,4} & J_{1,5} & J_{1,6} & J_{1,7} & J_{1,8} & J_{1,9} \\ 0 & 1 & 0 & J_{2,4} & J_{2,5} & J_{2,6} & J_{2,7} & J_{2,8} & J_{2,9} \\ 0 & 0 & 1 & 0 & J_{3,5} & J_{3,6} & J_{3,7} & J_{3,8} & J_{3,9} \\ 0 & 0 & 0 & 1 & J_{4,5} & J_{4,6} & J_{4,7} & 0 & J_{4,9} \\ 0 & 0 & 0 & 0 & J_{5,5} & J_{5,6} & J_{5,7} & 0 & J_{5,9} \\ 0 & 0 & 0 & 0 & J_{6,5} & J_{6,6} & J_{6,7} & 0 & J_{6,9} \end{bmatrix}$$

$$\begin{aligned}
J_{1,4} =& -(c\psi s\varphi - c\varphi s\psi s\theta)(L_1 + sq_1(L_4 + q_2) + \\
& L_5 s(q_1 + q_3) + L_2 cq_1 + L_3 sq_1) - c\theta s\psi(cq_1(L_4 + \\
& q_2) + L_5 c(q_1 + q_3) + L_3 cq_1 - L_2 sq_1) \\
J_{2,4} =& c\psi c\theta(cq_1(L_4 + q_2) + L_5 c(q_1 + q_3) + L_3 cq_1 - \\
& L_2 sq_1) - (s\varphi s\psi + c\varphi c\psi s\theta)(L_1 + sq_1(L_4 + q_2) + \\
& L_5 s(q_1 + q_3) + L_2 cq_1 + L_3 sq_1)
\end{aligned}$$

$$\begin{aligned}
J_{1,5} =& -c\psi s\theta(cq_1(L_4 + q_2) + L_5 c(q_1 + q_3) + L_3 cq_1 - \\
& L_2 sq_1) - c\varphi c\psi c\theta(L_1 + sq_1(L_4 + q_2) + \\
& L_5 s(q_1 + q_3) + L_2 cq_1 + L_3 sq_1) \\
J_{2,5} =& -s\psi s\theta(cq_1(L_4 + q_2) + L_5 c(q_1 + q_3) + L_3 cq_1 \\
& - L_2 sq_1) - c\varphi c\theta s\psi(L_1 + sq_1(L_4 + q_2) \\
& + L_5 s(q_1 + q_3) + L_2 cq_1 + L_3 sq_1) \\
J_{3,5} =& c\varphi s\theta(L_1 + sq_1(L_4 + q_2) + L_5 s(q_1 + q_3) + L_2 cq_1 \\
& + L_3 sq_1) - c\theta(cq_1(L_4 + q_2) + L_5 c(q_1 + q_3) \\
& + L_3 cq_1 - L_2 sq_1) \\
J_{4,5} =& (s(q_1 + q_3)s\varphi(c(q_1 + q_3)s\theta + s(q_1 + q_3)c\varphi c\theta))/ \\
& (c(q_1 + q_3)^2 c\theta^2 + s(q_1 + q_3)^2 s\varphi^2 + s(q_1 + q_3)^2 \\
& c\varphi^2 s\theta^2 - 2c(q_1 + q_3)s(q_1 + q_3)c\varphi c\theta s\theta) \\
J_{5,5} =& (c(q_1 + q_3)c\theta - s(q_1 + q_3)c\varphi s\theta)/(1 - (c(q_1 \\
& + q_3)s\theta + s(q_1 + q_3)c\varphi c\theta)^2)^{1/2} \\
J_{6,5} =& (s(q_1 + q_3)s\varphi)/(c\theta^2 + s(q_1 + q_3)^2 s\theta^2 - \\
& c\varphi^2 c\theta^2 + c(q_1 + q_3)^2 c\varphi^2 c\theta^2 - \\
& 2c(q_1 + q_3)s(q_1 + q_3)c\varphi c\theta s\theta)
\end{aligned}$$

$$\begin{aligned}
J_{1,6} =& -(c\varphi s\psi - c\psi s\varphi s\theta)(L_1 + sq_1(L_4 + q_2) \\
& + L_5 s(q_1 + q_3) + L_2 cq_1 + L_3 sq_1) \\
J_{2,6} =& (c\varphi c\psi + s\varphi s\psi s\theta)(L_1 + sq_1(L_4 + q_2) \\
& + L_5 s(q_1 + q_3) + L_2 cq_1 + L_3 sq_1) \\
J_{3,6} =& c\theta s\varphi(L_1 + sq_1(L_4 + q_2) + L_5 s(q_1 + q_3) \\
& + L_2 cq_1 + L_3 sq_1) \\
J_{4,6} =& (s\theta(c(q_1 + q_3)^2 - 1) + c(q_1 + q_3)s(q_1 + q_3)c\varphi c\theta)/ \\
& (c(q_1 + q_3)^2 c\theta^2 + s(q_1 + q_3)^2 s\varphi^2 + s(q_1 + q_3)^2 \\
& c\varphi^2 s\theta^2 - 2c(q_1 + q_3)s(q_1 + q_3)c\varphi c\theta s\theta) \\
J_{5,6} =& -(s(q_1 + q_3)c\theta s\varphi)/(1 - (c(q_1 + q_3)s\theta
\end{aligned}$$

$$
\begin{aligned}
&+ s(q_1+q_3)c\varphi c\theta)^2)^{1/2}\\
J_{6,6} =& (c\theta(c(q_1+q_3)c\theta - s(q_1+q_3)c\varphi s\theta))/(c\theta^2\\
&+ s(q_1+q_3)^2 s\theta^2 - c\varphi^2 c\theta^2 + c(q_1+q_3)^2 c\varphi^2 c\theta^2\\
&- 2c(q_1+q_3)s(q_1+q_3)c\varphi c\theta s\theta)
\end{aligned}
$$

$$
\begin{aligned}
J_{1,7} =& -(s\varphi s\psi + c\varphi c\psi s\theta)(cq_1(L_4+q_2) + L_5 c(q_1+q_3)\\
&+ L_3 cq_1 - L_2 sq_1) - c\psi c\theta(sq_1(L_4+q_2)\\
&+ L_5 s(q_1+q_3) + L_2 cq_1 + L_3 sq_1)\\
J_{2,7} =& (c\psi s\varphi - c\varphi s\psi s\theta)(cq_1(L_4+q_2) + L_5 c(q_1\\
&+ q_3) + L_3 cq_1 - L_2 sq_1) - c\theta s\psi(sq_1(L_4+q_2)\\
&+ L_5 s(q_1+q_3) + L_2 cq_1 + L_3 sq_1)\\
J_{3,7} =& s\theta(sq_1(L_4+q_2) + L_5 s(q_1+q_3) + L_2 cq_1 + L_3 sq_1)\\
&- c\varphi c\theta(cq_1(L_4+q_2) + L_5 c(q_1+q_3) + L_3 cq_1 - L_2 sq_1)\\
J_{4,7} =& (c\theta s\varphi)/(c(q_1+q_3)^2 c\theta^2 + s(q_1+q_3)^2 s\varphi^2\\
&+ s(q_1+q_3)^2 c\varphi^2 s\theta^2 - 2c(q_1+q_3)s(q_1+q_3)c\varphi c\theta s\theta)\\
J_{5,7} =& -(s(q_1+q_3)s\theta - c(q_1+q_3)c\varphi c\theta)/\\
&(1 - (c(q_1+q_3)s\theta + s(q_1+q_3)c\varphi c\theta)^2)^{1/2}\\
J_{6,7} =& (c\theta s\varphi(c(q_1+q_3)s\theta + s(q_1+q_3)c\varphi c\theta))/\\
&(c\theta^2 + s(q_1+q_3)^2 s\theta^2 - c\varphi^2 c\theta^2\\
&+ c(q_1+q_3)^2 c\varphi^2 c\theta^2 - 2c(q_1+q_3)s(q_1+q_3)c\varphi c\theta s\theta)
\end{aligned}
$$

$$
\begin{aligned}
J_{1,8} =& c\psi cq_1 c\theta - sq_1(s\varphi s\psi + c\varphi c\psi s\theta)\\
J_{2,8} =& sq_1(c\psi s\varphi - c\varphi s\psi s\theta) + cq_1 c\theta s\psi\\
J_{3,8} =& -cq_1 s\theta - c\varphi c\theta sq_1
\end{aligned}
$$

$$
\begin{aligned}
J_{1,9} =& -L_5 c(q_1+q_3)(s\varphi s\psi + c\varphi c\psi s\theta) - L_5 s(q_1+q_3)c\psi c\theta\\
J_{2,9} =& L_5 c(q_1+q_3)(c\psi s\varphi - c\varphi s\psi s\theta) - L_5 s(q_1+q_3)c\theta s\psi\\
J_{3,9} =& L_5 s(q_1+q_3)s\theta - L_5 c(q_1+q_3)c\varphi c\theta\\
J_{4,9} =& (c\theta s\varphi)/(c(q_1+q_3)^2 c\theta^2 + s(q_1+q_3)^2 s\varphi^2 +\\
&s(q_1+q_3)^2 c\varphi^2 s\theta^2 - 2c(q_1+q_3)s(q_1+q_3)c\varphi c\theta s\theta)\\
J_{5,9} =& -(s(q_1+q_3)s\theta - c(q_1+q_3)c\varphi c\theta)/\\
&(1 - (c(q_1+q_3)s\theta + s(q_1+q_3)c\varphi c\theta)^2)^{1/2}\\
J_{6,9} =& (c\theta s\varphi(c(q_1+q_3)s\theta + s(q_1+q_3)c\varphi c\theta))/\\
&(c\theta^2 + s(q_1+q_3)^2 s\theta^2 - c\varphi^2 c\theta^2 + c(q_1+q_3)^2 c\varphi^2 c\theta^2\\
&- 2c(q_1+q_3)s(q_1+q_3)c\varphi c\theta s\theta)
\end{aligned}
$$

Clarification: $c\psi^2$ means $\cos^2(\psi)$ for all sine and cosine terms.

A.4 Manipulator Jacobian

$$
J_{man} = \begin{bmatrix} J_{1,1} & J_{1,2} & J_{1,3} \\ J_{2,1} & J_{2,2} & J_{2,3} \\ J_{3,1} & J_{3,2} & J_{3,3} \\ 0 & 0 & 0 \\ 1 & 0 & 1 \\ 0 & 0 & 0 \end{bmatrix}
$$

$$
\begin{aligned}
J_{1,1} =& -sq_1(L_4+q_2) - L_5 s(q_1+q_3) - L_2 cq_1 - L_3 sq_1\\
J_{2,1} =& -L_5 s(q_1+q_3)\\
J_{3,1} =& L_2 sq_1 - L_5 c(q_1+q_3) - L_3 cq_1 - cq_1(L_4+q_2)\\
J_{1,2} =& cq_1\\
J_{2,2} =& -L_5 s(q_1+q_3)\\
J_{3,2} =& -sq_1\\
J_{1,3} =& -L_5 s(q_1+q_3)\\
J_{2,3} =& -L_5 s(q_1+q_3)\\
J_{3,3} =& -L_5 s(q_1+q_3)
\end{aligned}
$$

A.5 Link positions and rotations

The link positions denote the location and rotation of the center of mass of the respective link. The parameters a_{li} and b_{li} denote the distances of the origin of the link's frame in the previous joint's frame. The reference frames associated with each link have their origin located at the link center of mass with the axes following the link's principal axes (such that the cross-terms of the inertia tensor are zero). Because the principal axes of link 1 are not parallel to the axes of the frame at joint 1, it is rotated by r_{l1}. The parameters were determined from a CAD model of the manipulator.

Link 1

$$
\boldsymbol{p}_{l1}^b = \begin{bmatrix} b_{l1}cq_1 - a_{l1}sq_1 \\ 0 \\ -L_0 - a_{l1}cq_1 - b_{l1}sq_1 \end{bmatrix}
$$

$$
R_{l1}^b = \begin{bmatrix} c(q_1+r_{l1}) & -s(q_1+r_{l1}) & 0 \\ 0 & 0 & 1 \\ -s(q_1+r_{l1}) & -c(q_1+r_{l1}) & 0 \end{bmatrix}
$$

Link 2

$$
\boldsymbol{p}_{l2}^b = \begin{bmatrix} cq_1(a_{l2}+q_2) + L_2 cq_1 - L_1 sq_1 \\ 0 \\ -L_0 - sq_1(a_{l2}+q_2) - L_1 cq_1 - L_2 sq_1 \end{bmatrix}
$$

$$
R_{l2}^b = \begin{bmatrix} -sq_1 & 0 & cq_1 \\ 0 & 1 & 0 \\ -cq_1 & 0 & -sq_1 \end{bmatrix}
$$

Link 3

$$
\boldsymbol{p}_{l3}^b = \begin{bmatrix} cq_1(L_3+q_2) + \\ \quad a_{l3}c(q_1+q_3) + L_2 cq_1 - L_1 sq_1 \\ 0 \\ -L_0 - sq_1(L_3+q_2) - \\ \quad a_{l3}s(q_1+q_3) - L_1 cq_1 - L_2 sq_1 \end{bmatrix}
$$

$$
R_{l3}^b = \begin{bmatrix} cq_1 sq_3 + cq_3 sq_1 & cq_1 cq_3 - sq_1 sq_3 & 0 \\ 0 & 0 & 1 \\ cq_1 cq_3 - sq_1 sq_3 & -cq_1 sq_3 - cq_3 sq_1 & 0 \end{bmatrix}
$$

B

Simulation

This appendix contains additional information regarding the simulation experiments. The lengths of the members is reported in Table 5. The M, D and K matrices of the impedance filter are given in Equation 24. The table of PID gains used in the position controller is reported as Table 6. Additional results are shown in the figures of subsection B.1.

Table 5: Lengths of the members as used in the simulation.

Member	**Length [m]**
L_1	0.150
L_2	0.0375
L_3	0.015
L_4	0.532
L_5	0.027

$$M_d = \begin{bmatrix} 1 & 0 & 0 & 0 & 0 \\ 0 & 1 & 0 & 0 & 0 \\ 0 & 0 & 1 & 0 & 0 \\ 0 & 0 & 0 & 1 & 0 \\ 0 & 0 & 0 & 0 & 1 \end{bmatrix} \tag{24a}$$

$$D_d = \begin{bmatrix} 1 & 0 & 0 & 0 & 0 \\ 0 & 1 & 0 & 0 & 0 \\ 0 & 0 & 1 & 0 & 0 \\ 0 & 0 & 0 & 1 & 0 \\ 0 & 0 & 0 & 0 & 1 \end{bmatrix} \tag{24b}$$

$$K_d = \begin{bmatrix} 1 & 0 & 0 & 0 & 0 \\ 0 & 1 & 0 & 0 & 0 \\ 0 & 0 & 1 & 0 & 0 \\ 0 & 0 & 0 & 1 & 0 \\ 0 & 0 & 0 & 0 & 1 \end{bmatrix} \tag{24c}$$

Table 6: PID gains of the position controller implemented in the simulation.

Controller	**P**	**I**	**D**
X	0.2	0	0.3
Y	0.4	0	0.4
Z	35	0.6	17
ψ	100	0	50
θ	35	0	20
φ	25	0	30
q_1	60	5	25

B.1 Additional results

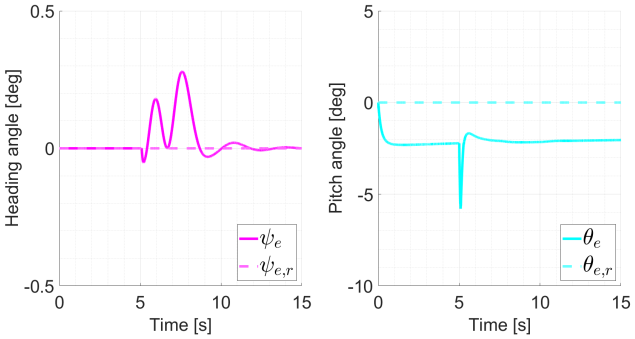

Figure 22: heading and pitch angles of the end-effector during the simulated position tracking mission.

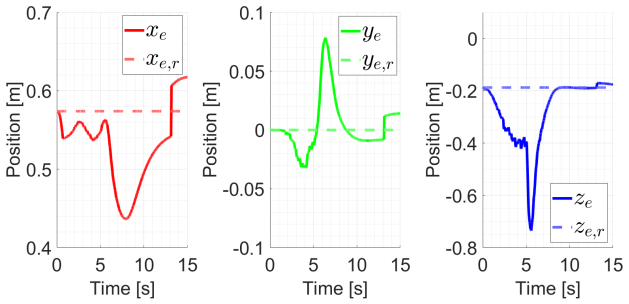

Figure 23: Position references and responses of the end-effector during simulated orientation tracking mission.

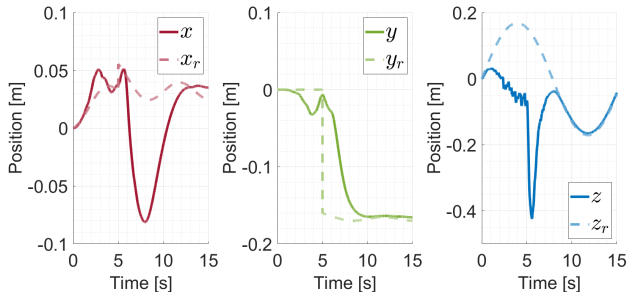

Figure 24: Position references and responses of the drone body during simulated orientation tracking mission.

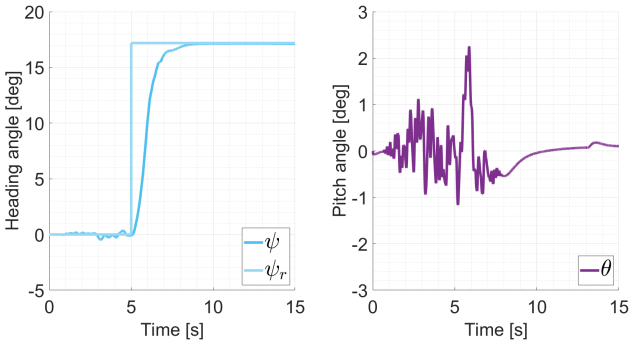

Figure 25: Orientation references and responses of the drone body during simulated orientation tracking mission.

C

Flight experiments

In this appendix, additional data related to the flight experiments are given. The impedance parameters used are given in Equation 25. Additional results are presented in subsection C.1

$$M_d = \begin{bmatrix} 1 & 0 & 0 & 0 & 0 \\ 0 & 1 & 0 & 0 & 0 \\ 0 & 0 & 1 & 0 & 0 \\ 0 & 0 & 0 & 1 & 0 \\ 0 & 0 & 0 & 0 & 1 \end{bmatrix} * k_M \tag{25a}$$

$$D_d = \begin{bmatrix} 1 & 0 & 0 & 0 & 0 \\ 0 & 1 & 0 & 0 & 0 \\ 0 & 0 & 1 & 0 & 0 \\ 0 & 0 & 0 & 1 & 0 \\ 0 & 0 & 0 & 0 & 1 \end{bmatrix} * k_D \tag{25b}$$

$$K_d = \begin{bmatrix} 1 & 0 & 0 & 0 & 0 \\ 0 & 1 & 0 & 0 & 0 \\ 0 & 0 & 1 & 0 & 0 \\ 0 & 0 & 0 & 1 & 0 \\ 0 & 0 & 0 & 0 & 1 \end{bmatrix} * k_K \tag{25c}$$

$$k_M = 1.0 \tag{25d}$$

$$k_K = 10.0 \tag{25e}$$

$$k_D = 2\sqrt{k_M * k_D} = 6.3 \tag{25f}$$

C.1 Additional results

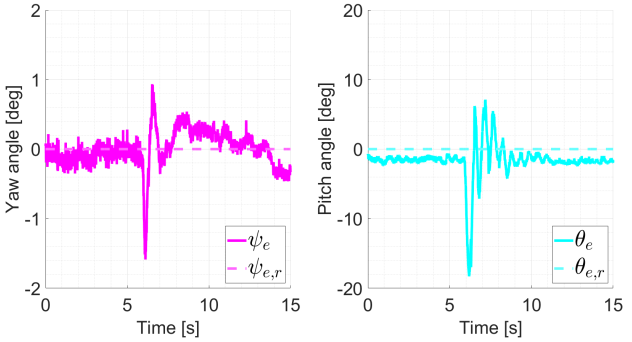

Figure 26: heading and pitch angles of the end-effector during the position tracking mission.

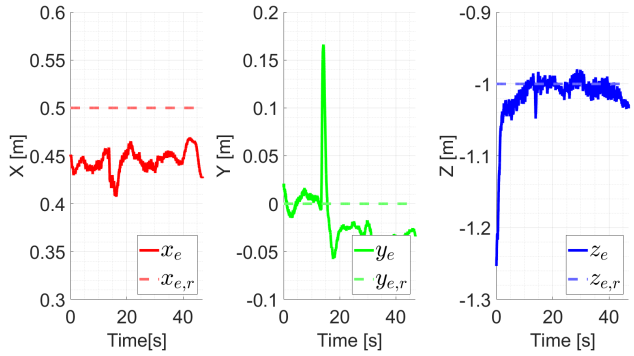

Figure 27: Position references and responses of the end-effector during orientation tracking mission.

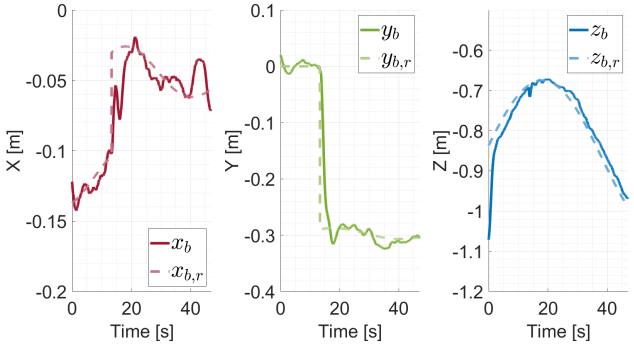

Figure 28: Position references and responses of the drone body during orientation tracking mission.

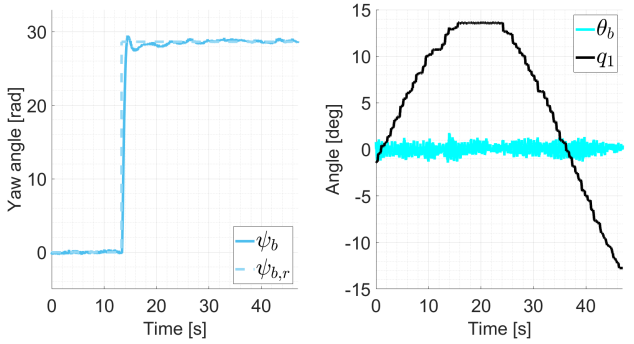

Figure 29: Orientation references and responses of the drone body during orientation tracking mission.